The Astrophysical Journal, 993:84 (21pp), 2025 November 1 https://doi.org/10.3847/1538-4357/ae0191

The Interstellar Medium in I Zw 18 Seen with JWST/MIRI. II. Warm Molecular Hydrogen and Warm Dust

L. K. Hunt[1], B. T. Draine[2], M. G. Navarro[3], A. Aloisi[4,5], R. J. Rickards Vaught[5], A. Adamo[6], F. Annibali[7], D. Calzetti[8], S. Hernandez[9], B. L. James[9], M. Mingozzi[9], R. Schneider[10,11,12,13], M. Tosi[7], B. Brandl[14,15], M. G. del Valle-Espinosa[5], F. Donnan[16], A. S. Hirschauer[17], M. Meixner[18], and D. Rigopoulou[16,19]

[1] INAF—Osservatorio Astrofisico di Arcetri, Largo E. Fermi 5, 50125 Firenze, Italy; leslie.hunt@inaf.it
[2] Department of Astrophysical Sciences, Princeton University, Princeton, NJ 08544, USA
[3] INAF—Osservatorio Astronomico di Roma, Via di Frascati 33, 00040 Monteporzio Catone, Italy
[4] Astrophysics Division, Science Mission Directorate, NASA Headquarters, 300 E Street SW, WA, DC 20546, USA
[5] Space Telescope Science Institute, 3700 San Martin Drive, Baltimore, MD 21218, USA
[6] Department of Astronomy, The Oskar Klein Centre, Stockholm University, AlbaNova, SE-10691 Stockholm, Sweden
[7] INAF—Osservatorio di Astrofisica e Scienza dello Spazio, Via Gobetti 93/3, 40129 Bologna, Italy
[8] Department of Astronomy, University of Massachusetts Amherst, 710 North Pleasant Street, Amherst, MA 01003, USA
[9] AURA for ESA, Space Telescope Science Institute, 3700 San Martin Drive, Baltimore, MD 21218, USA
[10] Dipartimento di Fisica, "Sapienza" Università di Roma, Piazzale Aldo Moro 2, I-00185 Roma, Italy
[11] INAF—Osservatorio Astronomico di Roma, Via di Frascati 33, I-00040 Monte Porzio Catone, Italy
[12] INFN, Sezione Roma1, Dipartimento di Fisica, "Sapienza" Università di Roma, Piazzale Aldo Moro 2, I-00185 Roma, Italy
[13] Sapienza School for Advanced Studies, Viale Regina Elena 291, I-00161 Roma, Italy
[14] Leiden Observatory, Leiden University, PO Box 9513, 2300 RA Leiden, The Netherlands
[15] Faculty of Aerospace Engineering, Delft University of Technology, Kluyverweg 1, 2629 HS Delft, The Netherlands
[16] Department of Physics, University of Oxford, Keble Road, Oxford, OX1 3RH, UK
[17] Department of Physics & Engineering Physics, Morgan State University, 1700 East Cold Spring Lane, Baltimore, MD 21251, USA
[18] Jet Propulsion Laboratory, California Institute of Technology, 4800 Oak Grove Dr., Pasadena, CA 91109, USA
[19] School of Sciences, European University Cyprus, Diogenes street, Engomi, 1516 Nicosia, Cyprus
Received 2025 May 27; revised 2025 August 27; accepted 2025 August 28; published 2025 October 30

Abstract

We present JWST/MIRI spectra from the Medium-resolution Spectrometer of I Zw 18, a nearby dwarf galaxy with a metallicity of ∼3% Solar. Here, we investigate warm molecular hydrogen, H_2, observed in spectra extracted in ∼120 pc apertures centered on eleven regions of interest. We detect seven H_2 rotational lines, some of which are among the weakest ever measured. The H_2 population diagrams are fit with local-thermodynamic-equilibrium models and models of photodissociation regions. We also fit the ortho-/para-H_2 ratios (OPRs); in three of the six regions for which it was possible to fit the OPR, we find values significantly greater than 3, the maximum value for local thermodynamic equilibrium. To our knowledge, although predicted theoretically, this is the first time that OPR significantly >3 has been measured in interstellar gas. We find that an OPR tends to increase with decreasing H_2 column density, consistent with the expected effects of self-shielding in advancing photodissociation fronts. The population diagrams are consistent with H nucleon densities of $\sim 10^5$ cm^{-3}, and an interstellar radiation field scaling factor, G_0, of $\sim 10^3$. This warm, dense H_2 gas coexists with the same highly ionized gas that emits [O IV] and [Ne V]. Emission from $T \gtrsim 50$ K dust is detected, including an as-yet-unidentified dust emission feature near 14 μm; possible identification of Al_2O_3 is discussed. The continuum emission from several regions requires that a considerable fraction of the refractory elements be incorporated in dust. Despite stacking spectra in the SE where H_2 is found, no significant emission from polycyclic aromatic hydrocarbons is detected.

Unified Astronomy Thesaurus concepts: Blue compact dwarf galaxies (165); Dwarf irregular galaxies (417); Interstellar medium (847); Infrared spectroscopy (2285)

1. Introduction

Metal-poor dwarf galaxies at redshifts near or beyond the epoch of reionization (EoR) are now being found routinely by JWST (e.g., L. J. Furtak et al. 2023; K. E. Heintz et al. 2023; J. E. Rhoads et al. 2023; J. R. Trump et al. 2023; E. Vanzella et al. 2023, 2024; T. Morishita et al. 2024). These galaxies are characterized by an intense star-formation rate (SFR) well above galaxies with similar mass locally, consistently with the evolution of the "main sequence" of star formation (L. J. Furtak et al. 2023; A. Calabrò et al. 2024). Given their high SFR, we would expect copious amounts of molecular gas to fuel their star-formation activity, but this is difficult to test, since no observations of H_2 in similar environments are yet available.

Although molecular hydrogen, H_2, is the most abundant molecule in the Universe, it is not directly observable in emission from cold gas. The rotational levels of H_2 are widely separated, with little or no thermal excitation in cold clouds. Fortunately, the heavier trace elements such as carbon and oxygen can combine in cold, dense clouds to form carbon monoxide, CO, with rotational lines that are easily excited. Thus, despite its low absolute abundance, $\sim 10^{-4}$ per H nucleon, CO has become the commonly used local proxy for H_2.

However, it is well known that in low-metallicity environments, CO is notoriously difficult to detect (P. M. Gondhalekar

et al. 1998; L. T. Barone et al. 2000; A. Leroy et al. 2007; D. Cormier et al. 2014; L. K. Hunt et al. 2014, 2015). This is mainly due to photodissociation of CO, because in metal-poor and dust-poor environments (e.g., E. F. van Dishoeck & J. H. Black 1988; A. D. Bolatto et al. 1999; M. G. Wolfire et al. 2010), it is relatively unshielded from the strong radiation field (RF) produced by massive stars. Consequently, the regions that contain CO shrink to the densest portions of the cloud, while other gas components such as singly ionized carbon C^+ and atomic carbon become more dominant (e.g., M. G. Wolfire et al. 2010).

It has been proposed that, in extremely metal-deficient environments, stars can form directly from cold atomic hydrogen, H I, rather than from the conversion of H I to dense molecular clouds (e.g., S. C. O. Glover & P. C. Clark 2012; M. R. Krumholz 2012). Such a process would be extremely important, given that H I tends to dominate the gas budget in the interstellar medium (ISM) at low metallicity locally (e.g., M. S. Bothwell et al. 2013; L. K. Hunt et al. 2020), and at high redshift (e.g., G. Popping et al. 2014; F. Walter et al. 2020).

JWST now offers the possibility to test the notion that star formation can occur in extremely low-metallicity environments without molecular gas. Here we present the JWST MIRI Medium-resolution integral field unit Spectrometer (MRS) observations of I Zw 18, a relatively close (18.2 Mpc) star-forming dwarf galaxy at $3\%\,Z_\odot$ ($12+\log\,(O/H)=7.18$, Y. I. Izotov et al. 1999), among the lowest metallicities in the nearby universe. Like the high-z dwarf galaxies, I Zw 18 is a starburst, with a stellar mass of $\sim10^6$–$10^7\,M_\odot$ (M. Fumagalli et al. 2010; S. C. Madden et al. 2014; S. Janowiecki et al. 2017; A. Nanni et al. 2020), an H I mass of $\sim10^8\,M_\odot$ (L. van Zee et al. 1998; F. Lelli et al. 2012), and an SFR estimated from the radio free–free continuum of $\sim0.2\,M_\odot\,\mathrm{yr}^{-1}$ (L. K. Hunt et al. 2005). The SFR is estimated to have been even larger over the last 10 Myr, $\gtrsim1\,M_\odot\,\mathrm{yr}^{-1}$ (F. Annibali et al. 2013; G. Bortolini et al. 2024). Consequently, we would expect significant H_2 emission if H_2 is, indeed, necessary for star formation.

Our JWST MIRI/MRS maps of I Zw 18 cover the two star-forming complexes in its main body (e.g., R. J. Dufour & J. J. Hester 1990). With JWST, we can characterize the H_2 content of I Zw 18 with high spatial definition, in an almost pristine environment similar to those of the dwarf galaxies newly discovered by JWST at or beyond the EoR. Our MIRI observations reveal high-ionization gas and H I recombination lines (L. K. Hunt et al. 2025, hereafter Paper I), as well as a full complement of warm H_2 transitions and dust continuum, but no detectable emission from polycyclic aromatic hydrocarbons (PAHs). In this paper, we focus on the H_2 and the dust emission. The observations, their reduction, and analysis are summarized in Section 2. We analyze the warm H_2 in Section 3 by fitting the population diagrams with empirical models, and also compare the population diagrams with state-of-the-art photodissociation region (PDR) models. Section 4 discusses the dust continuum and the detection of an unidentified dust emission feature near 14 μm; a search for PAH emission is described in Section 4.3. We discuss our results in Section 5 and summarize them in Section 6. Forthcoming papers will describe other aspects of the data including metallicity maps with [O IV] (R. J. Rickards Vaught et al. 2025, hereafter Paper III), emission-line maps (L. K. Hunt et al. 2025, in preparation), and inferred RF hardness from line-ratio maps (R. J. Rickards Vaught et al. 2025, in preparation).

2. MIRI/MRS Data and Analysis

We observed I Zw 18 on 2024 March 8 with the JWST MIRI/MRS (I. Argyriou et al. 2023) through the GO program #3353 (PI Aloisi/coPI Hunt). Two overlapping pointings were executed, each of ∼8 hr duration, so as to encompass both the NW and SE OB complexes in the main body; in an uninterruptible sequence, a separate background of the same duration was also observed. An orientation range for position angle of the dedicated background observations enabled us to acquire on-source MIRI imaging in F560W, F1130W, and F2550W to complement the filters acquired by GTO program #1233 (PI Meixner, see G. Bortolini et al. 2024; A. S. Hirschauer et al. 2024). All three MIRI gratings, SHORT, MEDIUM, and LONG, were observed, in order to provide spectral coverage from ∼5 to 28 μm with a spectral resolving power ranging from ∼ 1550 to 3250. A four-point dither pattern optimized for extended sources was employed, together with the SLOWR1 readout pattern, having 40 groups per integration and two integrations per exposure.

The MRS data were reduced using custom pipelines, adapted from the MIRI `jupyter` notebook using Calibration Reference Data System (CRDS) version 11.17.25 and context `jwst_1281.pmap`. These correspond to the latest calibrations given by D. R. Law et al. (2025). Because of the high signal-to-noise ratio (S/N) of the background observations, the background was subtracted in pixel-based mode (Stage 2) in order to better correct for localized spectral trends. The fringing correction was performed both according to the "standard" pipeline, but also in a subsequent customized script created for this purpose. For more details, see Paper I.

2.1. Convolved Cubes

The two pointings were combined with the `drizzle` method (D. R. Law et al. 2023) into a single set of cubes that consists of four channels, each conserving the native wavelength coverage and pixel sizes (e.g., 0.″13, 0.″17, 0.″20, 0.″35, for Channels 1, 2, 3, and 4, respectively). In order to determine the H_2 population diagrams, it was necessary to convolve the original data cubes to the point-spread function (PSF) at a longer wavelength. We chose to convolve to 18 μm, slightly redward of the longest wavelength of the H_2 transitions at $\lambda=17.03$ μm (see Table 2).

To achieve matched spatial resolution at 18 μm, we first assumed that the MIRI PSF is described by a Gaussian. The MIRI PSF full width half-maximum (FWHM) at each wavelength was then estimated according to D. R. Law et al. (2023, Equation (1)), and the final Gaussian kernel was calculated, assuming $\mathrm{FWHM}_\lambda=\sqrt{8\ln2}\,\sigma_\lambda$. The kernel width was defined as the quadrature difference for each λ plane in the cube, such that it has a width $\sigma=\sqrt{\sigma_{18}^2-\sigma_\lambda^2}$, where σ_λ is the intrinsic PSF σ at the wavelength of interest. These kernels were then convolved with the original cube to achieve 18 μm spatial resolution at all planes with $\lambda\leqslant18$ μm. Wavelength slices beyond 18 μm remain at their native resolution.

For the continuum fitting (Section 4), we instead constructed a new set of cubes, convolved to the 27 μm PSF. These are

Table 1
Aperture Centers for Spectral Extraction

Region	R.A. (J2000)	Decl.
NW	9:34:01.99	+55:14:27.3
VLA-NW-A	9:34:02.10	+55:14:28.1[a]
VLA-NW-B	9:34:01.85	+55:14:26.0[a]
VLA-NW-C	9:34:01.82	+55:14:29.1[a]
ULX-1	9:34:01.97	+55:14:28.4[b]
CO2-1	9:34:02.00	+55:14:28.8[c]
SE	9:34:02.29	+55:14:23.5
VLA-SE	9:34:02.36	+55:14:23.1[a]
JWST-SE-1	9:34:02.31	+55:14:24.1
JWST-SE-2	9:34:02.36	+55:14:22.6
JWST-SE-3	9:34:02.18	+55:14:23.2

Notes.
[a] J. M. Cannon et al. (2005).
[b] T. X. Thuan et al. (2004), J. Ott et al. (2005), R. J. Rickards Vaught et al. (2021).
[c] L. Zhou et al. (2021).

made in the same way as the 18 μm convolution, but for the $\lambda = 27$ μm PSF.

2.2. Aperture Spectra

Spectra were extracted from the convolved cubes with apertures having radii of 0.″65 (~120 pc diameter), centered on 11 regions of interest. The spectral stitching was performed in a customized script, followed by a one-dimensional (1D) residual fringe correction during the spectral extraction phase to remove high-frequency noise in Channels 3 and 4 (S. Kavanagh et al. 2024). Additional details are given in Paper I.

The regions of interest comprise the four VLA H II regions, denoted as VLA-NW-A, B, C, and VLA-SE, identified by the radio continuum maps with ~2″ beam presented by J. M. Cannon et al. (2005). They also cover the peak of the ^{12}CO(2–1) detection near the NW OB association by L. Zhou et al. (2021), and the ultraluminous X-ray source ULX-1 identified by T. X. Thuan et al. (2004). In addition, apertures were placed on the approximate centers of the NW and SE OB complexes. Visual inspection of the MIRI cubes showed four continuum sources. Three are near the VLA-SE H II region, although not exactly coincident with it. Thus, apertures for spectral extraction were also placed on the 14 μm peaks of this emission, denoted as JWST-SE-1, JWST-SE-2, and JWST-SE-3. The fourth 14 μm source is coincident with VLA-NW-A. These continuum sources are also visible in the MIRI images presented by A. S. Hirschauer et al. (2024), and discussed in Paper I. Table 1 reports the aperture centers used here (and in Paper I).

Figure 1 shows an RGB image of I Zw 18 with blue taken as the HST/ACS F606W image of I Zw 18 from A. Aloisi et al. (2007), but here realigned to the Gaia DR3 (Gaia Collaboration et al. 2021) astrometric system. The green color corresponds to the MIRI F560W, and the red to F1130W, both with a median background subtracted. The apertures shown in the right panel, centered on the regions of interest, are not independent, but this does not interfere with our goal of sampling a variety of individual regions with high S/N to assess differences in the properties of the H_2. The left panel of Figure 1 highlights clearly the presence of the reddish JWST-identified 14 μm continuum sources (Paper I). The gas filaments toward the NW are also evident both in the HST image (A. Aloisi et al. 2007) and in the MIRI F560W image, illustrated by the greenish-blue color of the emission.

As in Paper I, we opted for an aperture radius of 0.″65 as a compromise between encompassing more light and avoiding the danger of averaging over too many substructures within the aperture. J. Rigby et al. (2023) find that an aperture of 0.″65 radius encloses roughly 72% of the energy in the F1800W filter,[20] roughly the wavelength corresponding to the size of our convolution kernel. Although a larger aperture might be desirable, the smaller field of view (FoV) at shorter wavelengths results in incomplete spectra in the regions of interest close to the FoV border (see Figure 1). Our adopted aperture diameter of 1.″30 is twice the PSF FWHM of MIRI/MRS at the longest H_2 wavelength (17 μm). Because we use spectra extracted after convolution to a common PSF, our H_2 population diagrams should not be affected by resolution, unless there are dramatic variations in the H_2 excitation within the aperture.

Figure 2 shows the extracted spectra, over the spectral range of the H_2 lines, offset by arbitrary increments to enhance visibility. The original spectra are given by the light-gray curves, and the smoothed continua by the heavy colored ones, as reported in the legend; the zero level for each spectrum is illustrated as a horizontal dotted line. As in Paper I, we identified emission lines in the spectra automatically, using a custom script that relies on Python's `specutils/find_lines_threshold`. First, the piece-wise fitted continuum was subtracted from each spectrum; noise within these adjacent continuum regions was calculated for input to the line-finding algorithm. A S/N threshold of 3 was applied to identify potential line detections, and each of these line candidates was fit with the sum of a linear continuum and a Gaussian in a spectral window around the central wavelength. The rest-frame central wavelength of the best-fit Gaussian was then compared with known line lists, and a series of potential line detections was extracted for each spectrum. We inferred the total line flux by integrating the Gaussian, and estimated flux uncertainties by propagating the errors on the fitted parameters given by the Hessian matrix associated with the fit. Ultimately, a list of detected lines was computed by requiring n S/N $\geqslant 3$ on the fitted flux and by constraining the absolute value of the velocity offset to be $\leqslant 150$ km s^{-1}. Vertical dotted lines in Figure 2 show some of these identifications.

As stated in Paper I, the MIRI spectra of I Zw 18 show (S/N$\geqslant$3) detections for a total of 10 fine-structure lines, 15 H I recombination lines, and 7 H_2 transitions. In Paper I, we examined the ionized gas. Here we analyze the rotational H_2 transitions in spectra extracted from the convolved cubes. The detected H_2 line fluxes from the convolved cubes and their uncertainties are reported in Appendix A in Tables 5 and 6; Appendix A Figure 13 illustrates the fits of the H_2 lines and adjacent continua using the procedures described above.

3. Warm Molecular Hydrogen

One of the main motivations for our JWST/MIRI observations of I Zw 18, with a metallicity of ~3% $Z_\odot$, was to search for warm H_2 emission. As mentioned in Section 2.2, MIRI has

[20] See also https://jwst-docs.stsci.edu/jwst-mid-infrared-instrument/miri-performance/miri-point-spread-functions#gsc.tab=0.

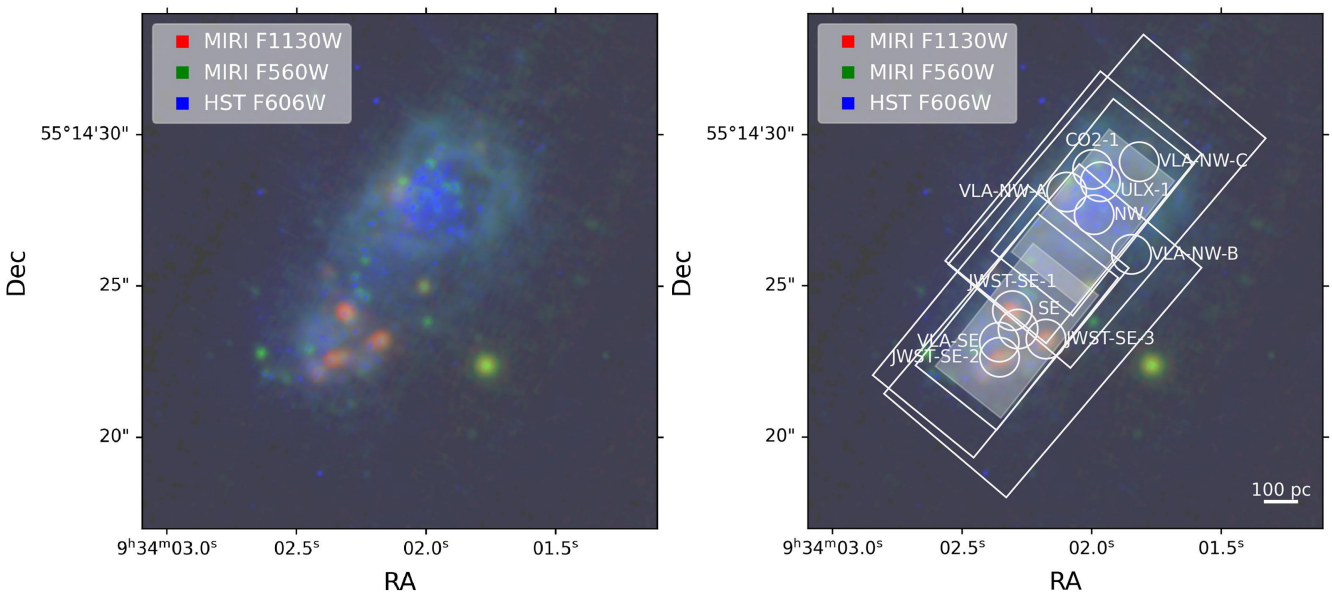

Figure 1. 17″ × 17″ RGB image of I Zw 18 showing the apertures of interest overlaid in the right panel. As in the legend, red is the MIRI F1130W background-subtracted image, green is the F560W background-subtracted image, and blue is the HST F606W image astrometrically corrected to Gaia. In the right panel, the circles illustrate the apertures (0.″65 radius, ∼120 pc diameter) for spectral extraction; the rectangles correspond to the MRS/IFU FoVs of the two separate pointings in the four channels. The smallest FoV, Channel 1, is illustrated by a transparent shading; the two pointings overlap allowing the construction of a complete spectral map even at the shortest wavelengths. The MIRI 14 μm continuum sources are apparent as red knots in the SE, and the faint knot in the NW associated with VLA-NW-A. The horizontal line in the lower right corner corresponds to 100 pc.

detected (with S/N $\geqslant 3$ and velocity offsets $\leqslant$150 km s^{-1}) 7 H_2 rotational transitions; here we model the resulting population diagrams as given in Table 2. These enable an estimation of the H_2 column density and the characterization of the properties of the emitting gas.

3.1. The Formalism

First, assuming optical thinness, the observed S(J) line flux is related to the H_2 column density N by:

$$F_J = \left(\frac{\Omega}{4\pi}\right) h\nu_J \, A_J \, N_{J+2}, \tag{1}$$

where ν_J is the frequency of the transition, Ω is the aperture solid angle, A_J is the probability per unit time of emission, and N_{J+2} is the associated column density. If we assume that the H_2 gas is in local thermodynamic equilibrium (LTE), namely with its excitation driven by collisions (this may not be true for the high-J transitions as we discuss in Section 3.7), then Boltzmann's equation relates the column density of a given H_2 level N_j to the total H_2 number column density $N_{\rm tot}$ through the gas temperature:

$$N_j = \frac{g_j}{Z(T)} N_{\rm tot} \exp(-E_j/kT) \tag{2}$$

where g_j is the degeneracy of upper state j, $Z(T)$ is the temperature-dependent partition function, E_j is the energy level of the upper state, k is Boltzmann's constant, and T is the kinetic temperature. The degeneracy g_j for even and odd values of j is given by:

$$g_j = \begin{cases} 2j+1 & \text{for even } j \text{ (para } -\text{);} \\ 3\,(2j+1) & \text{for odd } j \text{ (ortho } -\text{),} \end{cases} \tag{3}$$

since H_2 has two orientations of its coupled proton spins: one in which they are parallel (ortho-H_2), and one in which they are anti-parallel (para-H_2). In ortho-H_2, the total nuclear spin $F = 1$, so that the nuclear spin degeneracy $g_n = (2F + 1) = 3$.

Because ortho–para conversion is slow, para-H_2 and ortho-H_2 behave like distinct species. It is therefore useful to define separate rotational partition functions, Z, for para- and ortho-H_2:

$$Z(T_{\rm rot}) = \begin{cases} \sum\limits_{\text{even } j} (2j+1)\, e^{-E_j/kT_{\rm rot}} & \text{for even } j \text{ (para } -\text{);} \\ \sum\limits_{\text{odd } j} 3\,(2j+1)\, e^{-E_j/kT_{\rm rot}} & \text{for odd } j \text{ (ortho } -\text{).} \end{cases} \tag{4}$$

These summations can be approximated by simple analytic functions:

$$Z(T_{\rm rot}) \approx \begin{cases} \left[1 + \left(\frac{T}{170\ \rm K}\right)^4\right]^{1/4} & \text{for } Z_{\rm para}; \\ 9\, e^{-170\ K/T} + \dfrac{T}{57\ \rm K}\, e^{-510\ \rm K/T} & \text{for } Z_{\rm ortho}. \end{cases} \tag{5}$$

Following an empirical approach (N. L. Zakamska 2010; M. Pereira-Santaella et al. 2014; A. Togi & J. D. T. Smith 2016), we model the H_2 column densities using a continuous single power-law temperature T distribution such that

$$dN \propto T^{-n}\, dT, \tag{6}$$

for $T_l \leqslant T \leqslant T_u$, with T_l and T_u the lower and upper limits of the distribution, respectively; N is the column density, and n is the power-law index. Considering the continuous temperature distribution, we can derive a new expression for the relation of

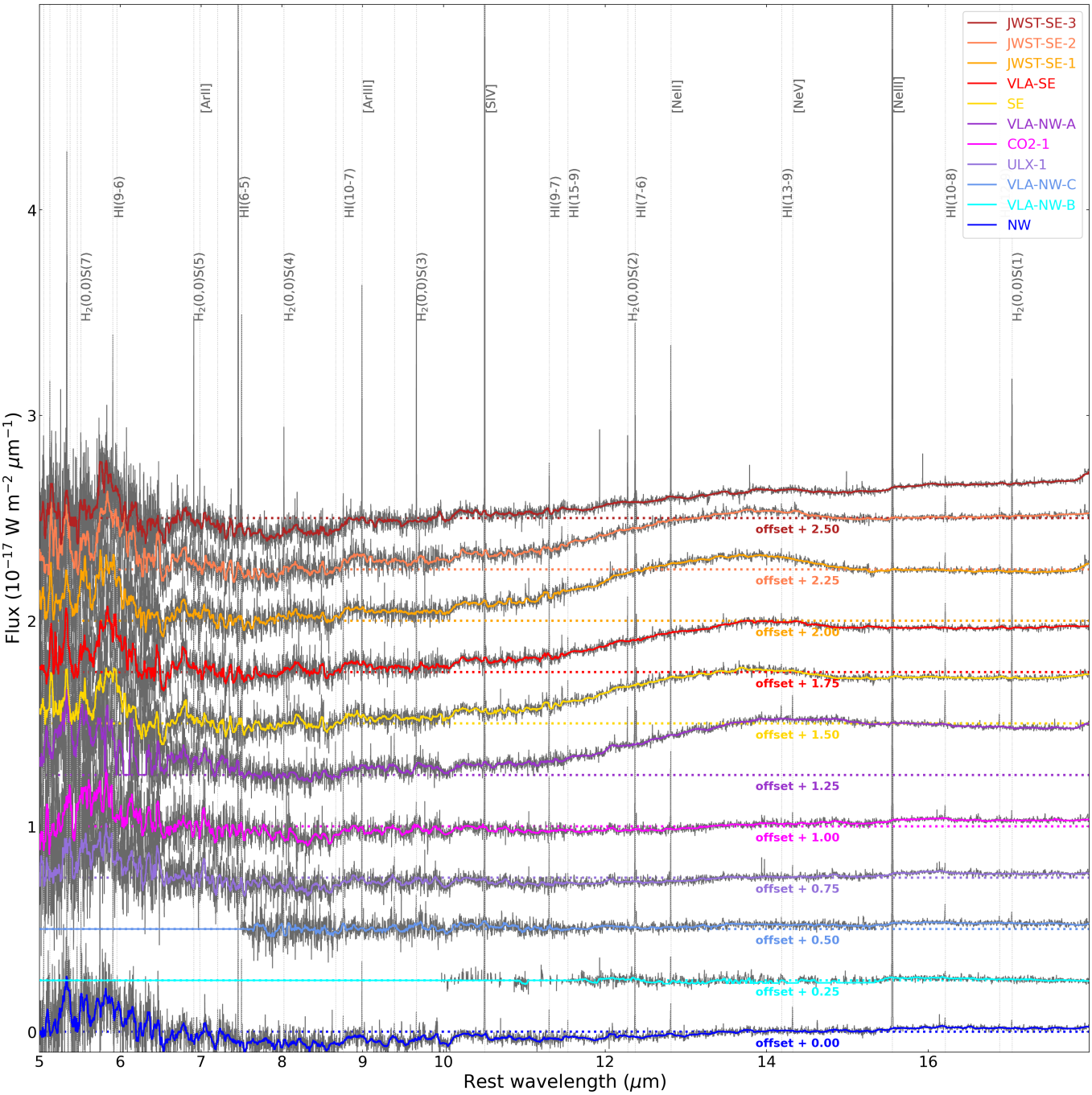

Figure 2. One-dimensional spectra extracted from the convolved cubes within the 0.″65-radius apertures shown in Figure 1. The vertical axis for flux density is in units of 10^{-17} W m^{-2} μm^{-1}, and the horizontal wavelength axis in μm; the horizontal axis has been restricted to show only the relevant H_2 lines. The gray curves show the spectra, while the heavy colored lines show the smoothed continua; the zero level for each spectrum is given as a horizontal dotted colored line. For better visibility of the spectra, the spectra are offset by small increments (in units of 10^{-17} W m^{-2} μm^{-1}) as denoted in the figure. The vertical dotted lines correspond to the detected transitions given in Tables 5 and 6; to avoid overcrowding, not all lines are labeled. The spectra for VLA-NW-B and VLA-NW-C are missing the short-wavelength MIRI channels because part of the aperture falls outside the MIRI FoV at those wavelengths.

the column density of the $i^{\rm th}$ transition with the total H_2 column $N_{\rm tot}$:

$$\frac{N_j}{g_j} = \left[\frac{(n-1)N_{\rm tot}}{T_l^{1-n} - T_u^{1-n}}\right] \int_{T_j}^{T_u} \frac{S_{\rm OPR}}{Z(T)} e^{\frac{-E_j}{kT}} T^{-n} dT \qquad (7)$$

where $Z(T)$ is given by Equation (5). With the ortho-/para-H_2 abundance ratio defined as OPR, $S_{\rm OPR}$ is the scaling factor for the column densities that takes into account the OPR, namely $S_{\rm OPR} = 1/(1+{\rm OPR})$ for para-H_2, and $S_{\rm OPR} = {\rm OPR}/(1+{\rm OPR})$ for ortho-H_2. H_2 in LTE has ${\rm OPR} = {\rm OPR}_{\rm LTE} = Z_{\rm ortho}(T)/Z_{\rm para}(T)$. In LTE at temperatures $T \lesssim 40$ K, H_2 is primarily in the ground state $J = 0$, so that $({\rm OPR})_{\rm LTE} \to 0$. In Equation (7), the implicit assumption is that the gas at different temperatures has the same OPR.

Operationally, by fixing OPR = 3, Equation (7) has four free variables, $N_{\rm tot}$, n, T_l, and T_u. To simplify the fit, we therefore assume a given T_u: in one set of fits $T_u = 2000$ K as used by

Table 2
MIRI H_2 Lines Used for Population Diagrams[a]

Transition	Notation	Rest Wavelength	E_u/k	A
$v = 0$		(μm)	(K)[b]	(10^{-10} s^{-1})[b]
$J = 3 \rightarrow 1$	S(1)	17.03485	1015	4.76
$J = 4 \rightarrow 2$	S(2)	12.27861	1681	27.55
$J = 5 \rightarrow 3$	S(3)	9.66491	2503	98.36
$J = 6 \rightarrow 4$	S(4)	8.02504	3473	264.3
$J = 7 \rightarrow 5$	S(5)	6.90951	4585	587.9
$J = 8 \rightarrow 6$	S(6)	6.10856	5828	1142
$J = 9 \rightarrow 7$	S(7)	5.51118	7196	2001
$J = 10 \rightarrow 8$	S(8)	5.05312	8677	3236

Notes.
[a] For completeness, we include the S(6) transition, even though it is not detected in I Zw 18 (see Tables 5, 6).
[b] Taken from E. Roueff et al. (2019).

A. Togi & J. D. T. Smith (2016) and others, and in another set $T_u = 3500$ K, in order to accommodate a potential excess of warm-hot H_2 in I Zw 18. We also normalize the fit to the brightest H_2 line, S(1); this leaves two free parameters in the fit, namely T_l and n. After fitting, it is straightforward to estimate the total H_2 column density $N_{\rm tot}$:

$$N_{\rm tot} = \frac{N_3}{(n-1)g_3}\,\frac{(1+{\rm OPR})}{\rm OPR}\,\frac{(T_l^{1-n}-T_u^{1-n})}{\int_{T_l}^{T_u} \frac{e^{\frac{-E_3}{kT}}\,T^{-n}dT}{Z_{\rm ortho}(T)}} \quad (8)$$

where N_3 is related to the integrated flux of S(1) through Equation (1). Finally, the total H_2 mass in the aperture can be calculated:

$$M_{\rm H2} = N_{\rm tot}\,\Omega\,D^2 m_{\rm H2}, \quad (9)$$

where D is the distance to I Zw 18, and $m_{\rm H2}$ is the mass of the H_2 molecule.

3.2. Fitting Procedures

The fits were applied only to those apertures where at least five H_2 transitions were detected with S/N $\geqslant 3$: JWST-SE-1, JWST-SE-2, JWST-SE-3, SE, VLA-SE, and VLA-NW-A. All five regions in the SE were detected in five or more H_2 transitions, while, toward the NW, this was true only for VLA-NW-A. Notably, the aperture centered on the CO(2–1) detection did not satisfy this criterion.[21] Because of the low extinction in I Zw 18 (see Paper I), we have not applied any extinction correction to the H_2 lines before fitting.

We estimated the best-fit parameters T_l and n by minimizing χ^2, or equivalently, maximizing the likelihood $L \propto \exp^{-\chi^2/2}$, assuming Gaussian errors. χ^2 is calculated using the model given in Equation (7), and the data and their uncertainties in Tables 5 and 6 (Appendix A) are plugged into Equation (1). To do this, we used a direct minimization with the Python package `SciPy/minimize`, and explored the parameter space to estimate the uncertainties and mutual correlations of the best-fit parameters with the Markov Chain Monte Carlo (MCMC) package `emcee` (D. Foreman-Mackey et al. 2013). This package is a Python implementation of the affine invariant MCMC ensemble sampler designed for parameter estimation by J. Goodman & J. Weare (2010). Uniform priors are adopted for both T_l and n; in particular, we confined T_l to be $\geqslant$50 K.

The integrated intensities of the S(1) lines in I Zw 18 are among the faintest ever measured; they range from the brightest in JWST-SE-3, 1.0×10^{-9} W m^{-2} sr^{-1}, to the faintest in the CO2–1 aperture, 8.1×10^{-11} W m^{-2} sr^{-1}, a factor of 8 below the S(1) intensity of 6.3×10^{-10} W m^{-2} sr^{-1} measured in Leo P, a nearby faint dwarf irregular also at $\sim$3% $Z_\odot$ (O. G. Telford et al. 2024), but powered by just one O star (C. J. Evans et al. 2019).[22]

3.3. Results with Fixed OPR

Here we report on the fits with $T_u = 2000$ K; similar results for $T_u = 3500$ K are given in Appendix B, where we also compare the best-fit parameters from the two sets of fits. The results are shown in Figure 3 as blue curves where N_j/g_j normalized to S(1) (N_3/g_3) is plotted against E_i. The best-fit parameters with the MCMC 1σ uncertainties are given in Table 3. Figure 4 shows the probability distribution function (PDF) of the fitted parameters in the upper and right panels for each region, and the mutual dependence of T_l and n in the lower left panels. As the nominal best-fit value, we have used the initial minimization, rather than the mode or median of the posterior PDF, which however, usually coincide (the exceptions are n for JWST-SE-1 and VLA-NW-A, where the mode of the PDF is skewed toward low values of n). The uncertainties correspond to the 16% and 84% percentiles of the posterior PDF distribution. The uncertainties on $N_{\rm tot}$ and H_2 mass have been calculated by randomly sampling 1000 times the joint posterior PDF distribution of the fitted parameters, computing log ($N_{\rm tot}$) for each sample, and taking the standard deviation of the result.

We have assessed the quality of the two sets of fits with different T_u, according to the Akaike information criterion (AIC; H. Akaike 1974) and the Bayesian information criterion (BIC, see Table 3 and Table 7 in Appendix B), and find that there is no clear statistical difference between the two sets of fits. In three of the regions, the AIC would point to $T_u = 2000$ K as being a better fit, and the other three to $T_u = 3500$ K.

Figure 4 shows significant covariance of the parameters T_l and n (with $T_u = 2000$ K) for each of the regions in I Zw 18, unlike the majority of the galaxies analyzed by A. Togi & J. D. T. Smith (2016, see their Figures 3 and 6),[23] which showed little covariance. In their case, n is practically independent of T_l, especially toward lower T_l. Similarly, in JWST-SE-1 and VLA-NW-A, the trend between T_l and n flattens at low T_l, which suggests that under such conditions, the best-fit parameters are not easy to determine, unless methods like the MCMC used here are employed. Because T_l is well determined for I Zw 18, we speculate that the bulk of I Zw 18's warm H_2 content is traced by the MIRI rotational lines.

Just as in more massive galaxies (e.g., M83, NGC 5728, NGC 7469: T. S. Y. Lai et al. 2022; S. Hernandez et al. 2023; R. Davies et al. 2024, respectively), the MIRI H_2 population diagrams of I Zw 18 are well approximated by a continuous temperature distribution. However, the massive galaxies have

[21] This may partially be due to a small fraction of the aperture falling outside the Channel 1 FoV (see Figure 1).

[22] Their photometric aperture has a diameter roughly half of ours, 0.″67.

[23] A. Togi & J. D. T. Smith (2016) used Spitzer/IRS data for which S(0) is available, which may influence this finding.

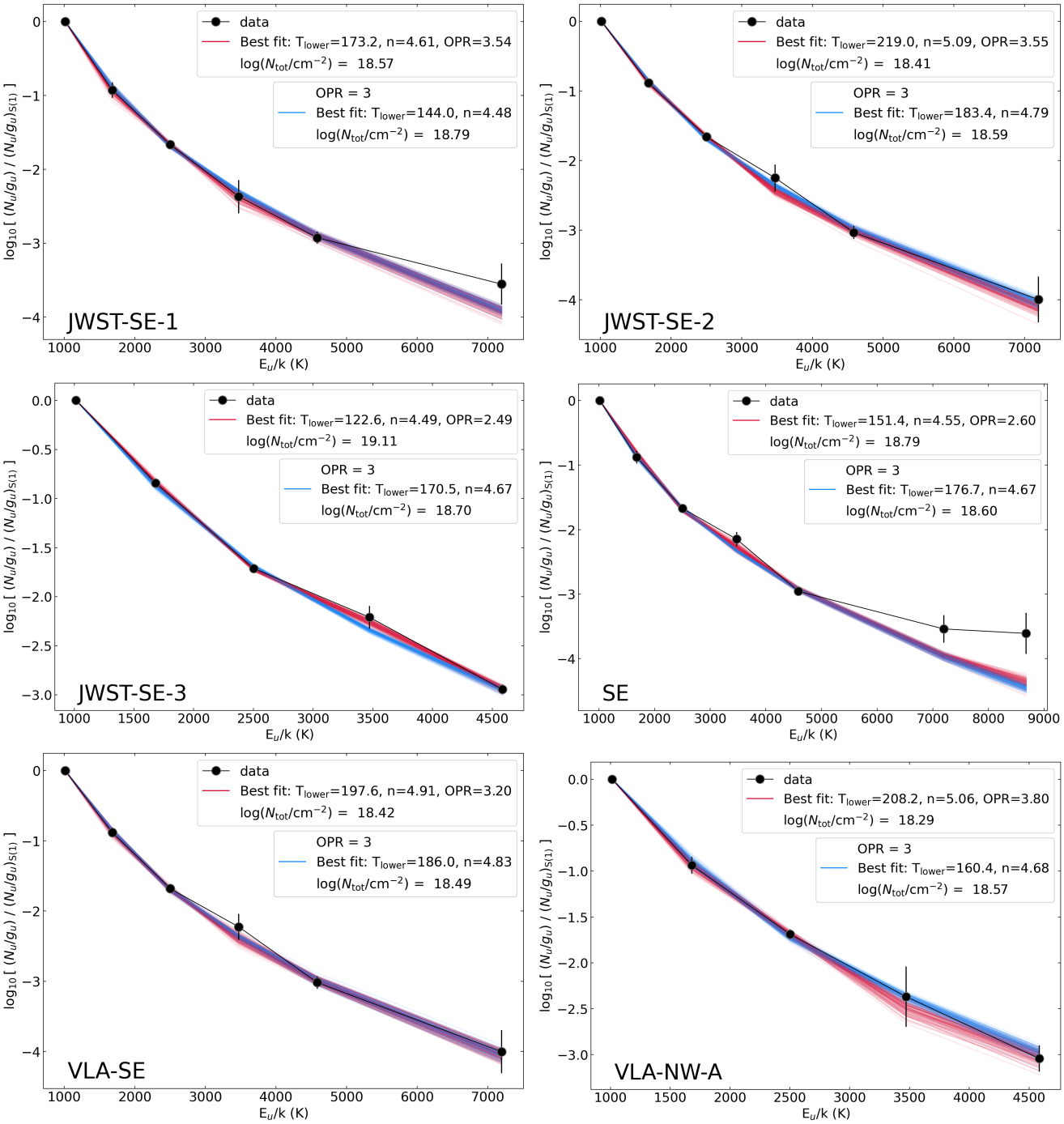

Figure 3. Molecular hydrogen population diagrams for the apertures with five or more H_2 detections at a 3σ level or greater, together with the best-fit models with $T_u = 2000$ K. Fits with OPR = 3 letting T_l and n vary are shown as blue curves, according to the MCMC sampler spread; the analogous fits letting OPR, T_l and n vary are shown as red curves (see Section 3.4). The total H_2 column density shown in the legends is given by Equation (8).

steeper power-law indices ($n = 4.9$–6.3) and warmer T_l for the integral ($T_l \sim 250$–300 K), compared to the results shown in Table 3. The generally shallower indices $n < 5$ for I Zw 18 (and in the nucleus and "hot spot" in NGC 5728, R. Davies et al. 2024) imply a greater fraction of warm H_2 that emits at higher temperatures.

The fitted warm H_2 column densities (see Table 3) are more than an order of magnitude lower than $N_{\rm tot} \sim 10^{20}$–10^{21} cm^{-2}, typical of spiral disks (e.g., E. Schinnerer & A. K. Leroy 2024). They are also much lower than the implied H_2 columns from resolved CO molecular clouds at pc scales in two low-metallicity dwarf galaxies, WLM and Sextans B (M. Rubio et al. 2015; Y. Shi et al. 2020, respectively); the CO measurements typically probe the highest H_2 column within the cloud (e.g., A. D. Bolatto et al. 2013). As reported in Table 3, the implied H_2 mass within the 120 pc apertures ranges from $\sim$300 $M_\odot$ to $\sim$2000 $M_\odot$. The highest of these are close to the range of virial cloud masses of 10^3–10^4 $M_\odot$ found in WLM ($\sim$13% $Z_\odot$) and Sextans B ($\sim$7% $Z_\odot$) by M. Rubio et al. (2015), Y. Shi et al. (2020), respectively.

The results from the population diagrams imply that the molecular gas in I Zw 18 is sufficiently dense to thermalize the

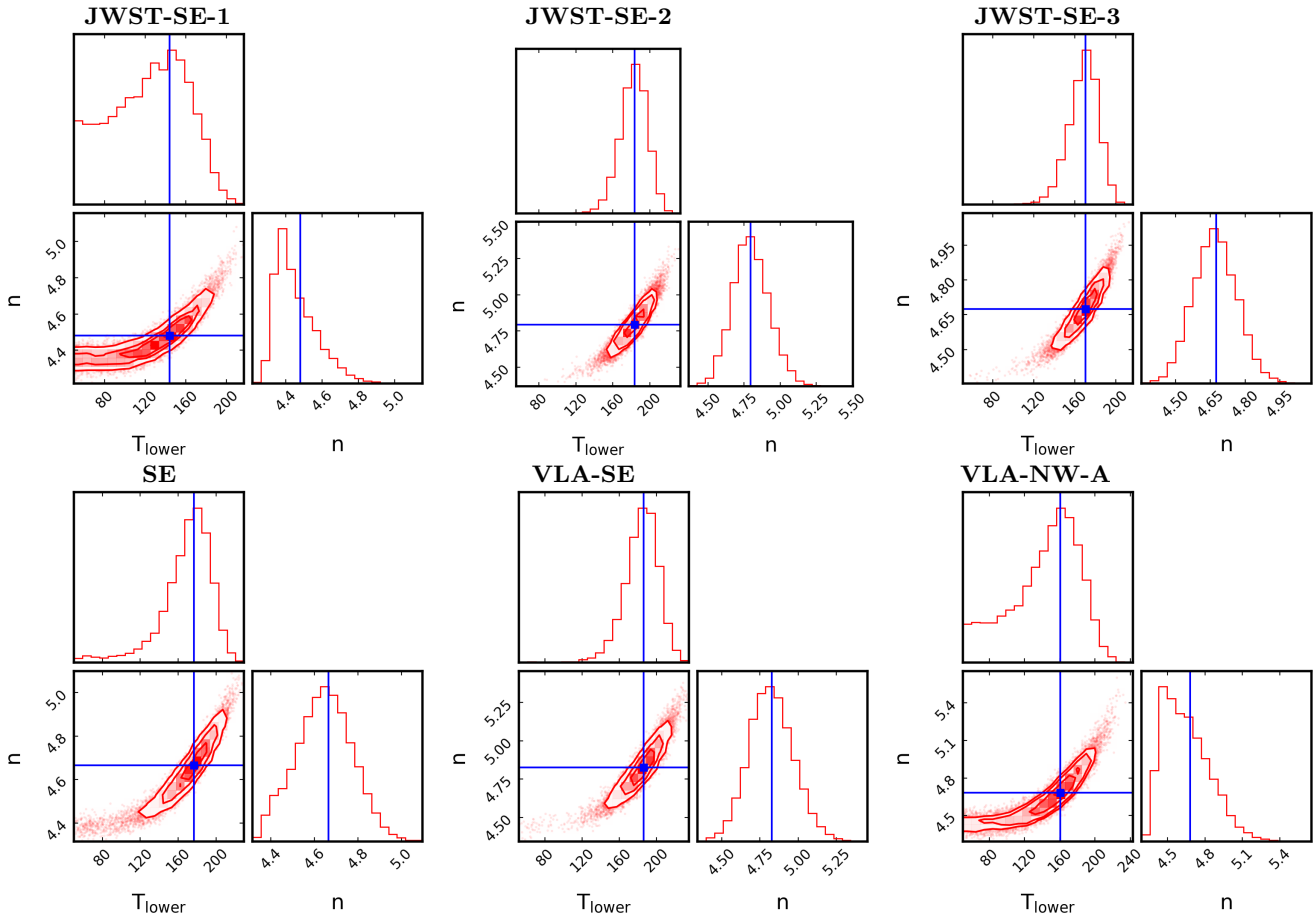

Figure 4. Corner plots for the (T_l, n) fits of the H_2 population diagrams with $T_u = 2000$ K. For each region, the upper and right panels show the PDF, and the lower left panel shows the co-dependence of the two parameters. It can be seen that T_l and n are correlated, with an extension toward flatness particularly pronounced in JWST-SE-1 and VLA-NW-A.

Table 3
Best-fit Results for H_2 Population Diagrams with $T_u = 2000$ K

Region	Number points	Max J_{up}	T_l (K)	n	OPR	$\log_{10}$ (N_{tot}/cm^{-2})[a]	$\log_{10}$ ($H_2/M_\odot$)[b]	AIC[c]	BIC[d]	χ^2
(1)	(2)	(3)	(4)	(5)	(6)	(7)	(8)	(9)	(10)	(11)
OPR = 3										
JWST-SE-1	6	9	144^{+48}_{-35}	$4.48^{+0.08}_{-0.15}$	⋯	18.79 ± 0.45	3.01 ± 0.45	4.97	4.55	7.05
JWST-SE-2	6	9	183^{+15}_{-14}	$4.79^{+0.12}_{-0.13}$	⋯	18.59 ± 0.09	2.81 ± 0.09	6.34	5.93	8.87
JWST-SE-3	5	7	171^{+15}_{-13}	$4.67^{+0.09}_{-0.10}$	⋯	18.70 ± 0.10	2.92 ± 0.10	6.53	5.75	8.29
SE	7	10	177^{+27}_{-19}	$4.67^{+0.13}_{-0.13}$	⋯	18.60 ± 0.26	2.82 ± 0.26	13.32	13.21	26.50
VLA-SE	6	9	186^{+19}_{-16}	$4.83^{+0.14}_{-0.15}$	⋯	18.49 ± 0.17	2.70 ± 0.17	1.93	1.51	4.25
VLA-NW-A	5	7	160^{+51}_{-30}	$4.68^{+0.16}_{-0.22}$	⋯	18.57 ± 0.43	2.79 ± 0.43	3.48	2.70	4.51
Fitting OPR										
JWST-SE-1	6	9	173^{+48}_{-29}	$4.61^{+0.17}_{-0.19}$	$3.54^{+0.38}_{-0.45}$	18.57 ± 0.36	2.79 ± 0.36	4.74	4.11	4.86
JWST-SE-2	6	9	219^{+19}_{-17}	$5.09^{+0.19}_{-0.21}$	$3.55^{+0.25}_{-0.26}$	18.41 ± 0.08	2.63 ± 0.08	3.74	3.12	4.12
JWST-SE-3	5	7	123^{+39}_{-35}	$4.49^{+0.04}_{-0.10}$	$2.49^{+0.13}_{-0.16}$	19.11 ± 0.49	3.33 ± 0.49	−0.15	−1.33	1.46
SE	7	10	151^{+54}_{-36}	$4.55^{+0.09}_{-0.16}$	$2.60^{+0.23}_{-0.27}$	18.79 ± 0.47	3.01 ± 0.47	14.83	14.66	24.70
VLA-SE	6	9	198^{+28}_{-21}	$4.91^{+0.20}_{-0.20}$	$3.20^{+0.32}_{-0.32}$	18.42 ± 0.25	2.64 ± 0.25	3.23	2.61	3.78
VLA-NW-A	5	7	208^{+34}_{-25}	$5.06^{+0.31}_{-0.34}$	$3.80^{+0.44}_{-0.47}$	18.29 ± 0.25	2.50 ± 0.25	−4.85	−6.02	0.57

Notes.
[a] Calculated from Equation (8).
[b] Calculated from Equation (9).
[c] Calculated according to `SciPy/optimize`: AIC = $N \ln(\chi^2/N) + 2N_{fit}$ where N_{fit} is the number of fitted parameters, and N is the number of data points.
[d] Calculated according to `SciPy/optimize`: BIC = $N \ln(\chi^2/N) + \ln(N)N_{fit}$.

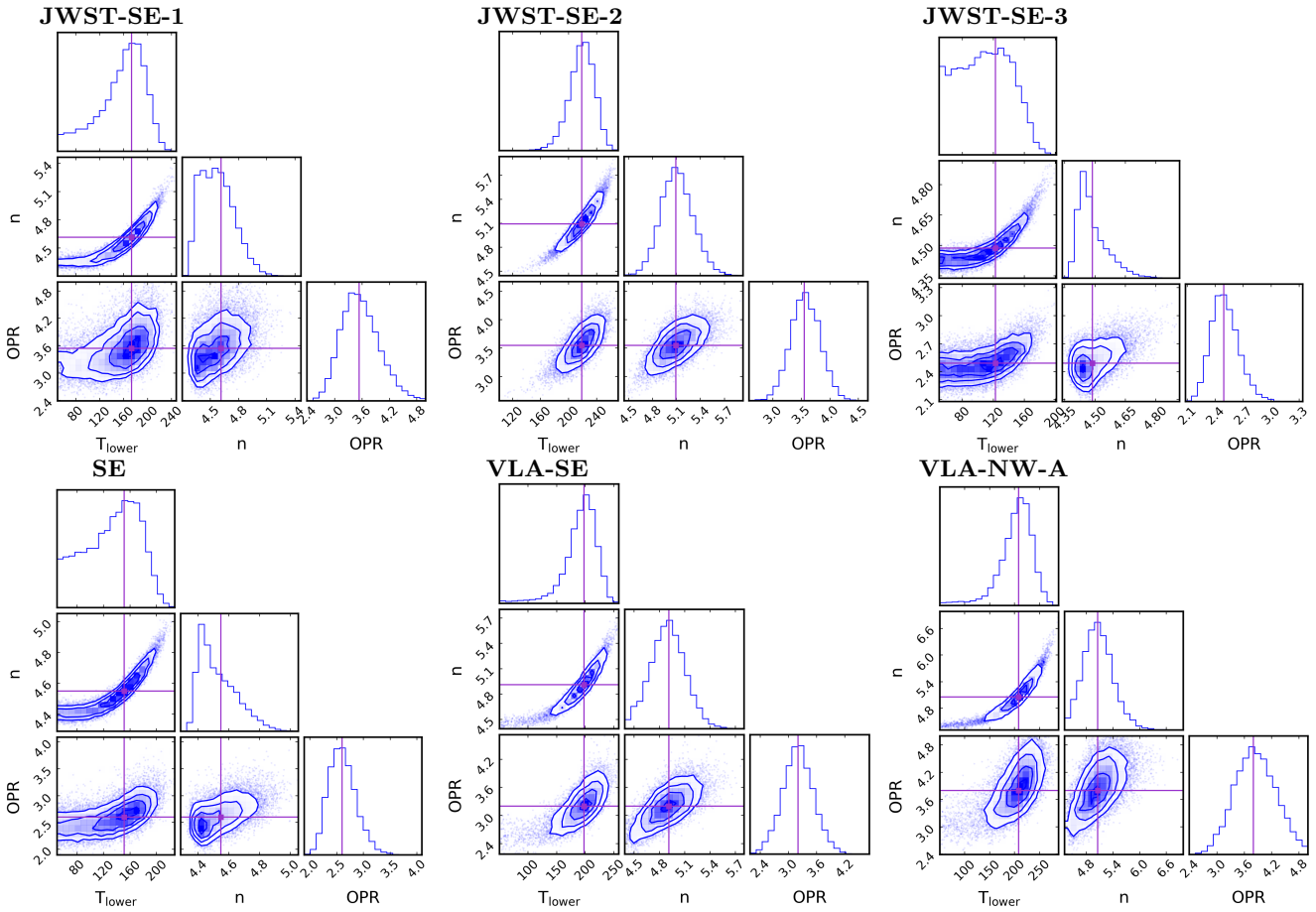

Figure 5. Corner plots for the (T_l, n, OPR) fits of the H_2 population diagrams with $T_u = 2000$ K. As in Figure 4, for each region, the top and right-most panels show the PDF, and the lower corner panels show the co-dependence of the three parameters. As in Figure 4, T_l and n are correlated, but here the OPR is also correlated with T_l and n, with a tendency toward flatness (lower left subpanels) in JWST-SE-3 and SE; these are also the regions where OPR < 3.

S(5) line, with a critical density of $\sim 10^5\,\mathrm{cm}^{-3}$ (e.g., B. T. Draine 2011), denser than the ionized gas with electron densities $\sim 10^2\,\mathrm{cm}^{-3}$ judging from the optical (Y. I. Izotov et al. 1999)[24] and the thermal radio continuum (L. K. Hunt et al. 2005). The detections of the high-J lines suggest that the warm molecular clouds in I Zw 18 are characterized by relatively high densities, typical of the cooler clouds probed by CO. We quantify this below in Section 3.5. The lowest H_2 rotational lines (e.g., S(1)) mainly originate in cooler gas ($T \lesssim 200$ K), while higher-J lines need warmer temperatures ($T \gtrsim 400$ K) and densities high enough ($n_\mathrm{H} \gtrsim 10^5\,\mathrm{cm}^{-3}$) to thermalize the levels. As discussed below in Section 3.7, H_2 is excited by collisions and UV pumping (e.g., B. T. Draine 2011), and the trade-off between excitation and self-shielding can be assessed through H_2 excitation diagrams like those in Figure 3. The total H_2 column densities, N_tot, are sufficiently high to provide significant levels of self-shielding.

3.4. Fitting the OPR

It can be seen from Figure 3 that some of the high-J lines are not well fit by our empirical model. This could be due to non-LTE processes exciting the lines, such as UV pumping, which we will discuss in Sections 3.5 and 3.7, but also to our assumption about a fixed OPR = 3. Thus, we have extended the LTE model to include a third variable, the OPR. This reduces the constraints on the fits by introducing an additional variable, but, with at least five H_2 transitions considered, it is feasible.

As for the previous fits, uniform MCMC priors are adopted for T_l, n, and OPR, with T_l constrained to be $\geqslant 50$ K; we also repeated the fitting procedure for both $T_u = 2000$ K and $T_u = 3500$ K. The new fits including the OPR (with $T_u = 2000$ K) are shown in Figure 3 as red curves, and the best-fit parameters are reported in the bottom portion of Table 3. Figure 5 gives the corner plots from the MCMC sampling. As before, we have taken the best-fit values to be those that come from the χ^2 minimization, and, in general, they coincide with the mode and median of the posterior PDFs. This is not the case for n in the SE aperture, where the PDF extends to lower values. When fitting also the OPR, the uncertainties on T_l are generally larger than when OPR is fixed. Nevertheless, comparing the AIC of the fits with and without fitting the OPR suggests that the variable OPR fits are generally the more statistically valid representation of the data; in particular, the fits where OPR > 3 are always superior from this perspective.

Appendix B reports the results of the H_2 population diagram fits with $T_u = 3500$ K, with and without fitting the OPR. Higher T_u gives higher values of T_l and n, thus slightly lower values of N_tot and H_2 mass within the aperture. The left panel of Figure 6 illustrates the comparison of the estimates of N_tot and H_2 mass, considering the two T_u values and with/

[24] Densities of the ionized gas are discussed in detail in Paper III.

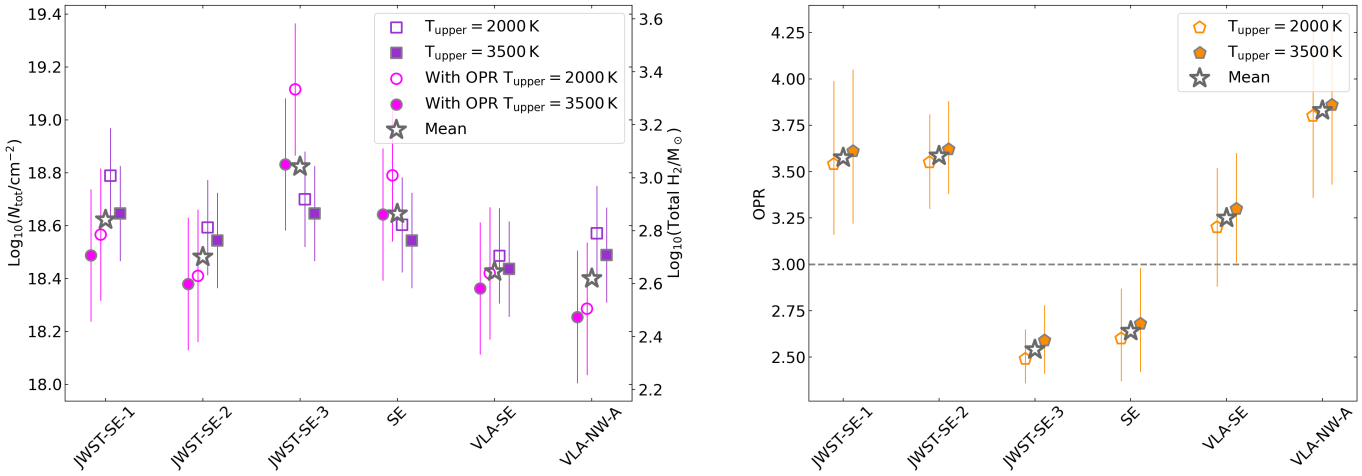

Figure 6. Left panel: Comparisons of the H_2 column N_{tot} and H_2 total mass inferred from fits at different T_u, and also with and without fitting the OPR. The left-hand ordinate scale shows H_2 column density, and the right H_2 total mass within the apertures. Right panel: Comparison of OPR inferred from fits with different T_u. The open star shows the mean for each region. In the right panel, the horizontal dashed line indicates the maximum LTE value of OPR = 3.

without fitting the OPR; the right panel shows the comparison with T_u of the best-fit OPR. Both N_{tot} and H_2 mass are well constrained, showing relatively little variation among the four sets of fits. The value of the fitted OPR also does not vary significantly with T_u; the root-mean-square difference of the best-fit OPR for the two values of T_u is only 0.08, thus reinforcing the significance of the OPR values >3 and <3 resulting from our analysis. For more details, see Appendix B.

From Figure 3, it is evident that although the lowest H_2 transitions from S(1) to S(5) are well fit by this simple model, the higher J transitions, S(7) in JWST-SE-1 and SE (as well as S(8) in SE), tend not to be. We attribute this to an increasing contribution of non-LTE processes such as UV pumping to the higher J levels (Section 3.7), or simply to the failure of the simple power-law model (Equation (6)) to describe the actual temperature distribution. More high-J rotational lines or lines from vibrationally excited levels would be needed to substantiate this hypothesis.

3.4.1. Best-fit OPR > 3

The corner plots in Figure 5 show that for three regions, JWST-SE-1, JWST-SE-2, and VLA-NW-A, the models significantly favor a best-fit OPR > 3. These three apertures are spatially independent, so we are sampling similar physical conditions in different regions of the galaxy. Although the possibility of OPR > 3 was predicted theoretically by B. T. Draine & F. Bertoldi (1996) and A. Sternberg & D. A. Neufeld (1999), this is the first time that an OPR > 3 has been measured in the ISM of any star-forming region.

The H_2 OPR is a variable arising from a complex interplay of competing physical processes. The true OPR in a PDR depends on temperature, collisions of H_2 with protons and hydrogen atoms, selective photodissociation of ortho- and para-H_2, the H_2 formation rates, and the efficiency of grain-surface reactions (e.g., A. Sternberg & D. A. Neufeld 1999; E. Bron et al. 2016). In star-forming galaxies with metallicities comparable to Solar, H_2 formation is dominated by catalysis on grain surfaces; this process is expected to create H_2 molecules with an OPR ≈ 3. There is also H_2 production in the gas phase via $H^- + H \rightarrow H_2 + e^-$, but in chemically evolved galaxies, this process is very subdominant compared to grain catalysis. However, in very metal-poor systems, gas-phase production will be the dominant channel. Because the gas-phase reaction is relatively indifferent to the H_2 proton spins, this process is also expected to produce H_2 with an OPR ≈ 3.

A higher OPR > 3 could arise through effective self-shielding, since the dominant process for H_2 destruction is photodissociation. If OPR > 1, ortho-H_2 self-shields more effectively than para-H_2. Preferential destruction of para-H_2 acts to increase OPR. In a stationary PDR, photodissociation and H_2 formation are balanced, and ortho → para conversion tends to be fast enough to keep OPR $\lesssim$ 3. However, when an increase in the far-ultraviolet (FUV) flux causes the photodissociation rate to exceed the local H_2 formation rate, a photodissociation front will propagate rapidly into the H_2 gas.

In a low-metallicity galaxy like I Zw 18, the highly suppressed rate for H_2 formation on dust grains will result in rapidly propagating photodissociation fronts, leading to an increase in the OPR. JWST-SE-1, JWST-SE-2, and VLA-NW-A, with OPR >3, may be regions where molecular gas is being irradiated by recently formed OB stars, with preferential destruction of para-H_2 causing OPR to increase beyond 3. In such a case, we might expect lower total H_2 column densities where OPR > 3. Figure 7 shows the OPR for each region plotted against the total H_2 column N_{tot}. Indeed, except for VLA-SE, which overlaps significantly with SE and JWST-SE-2, the trend of increasing OPR with decreasing N_{tot} is essentially monotonic, consistent with OPR >3 resulting from selective photodissociation.

3.4.2. Best-fit OPR $\lesssim$ 3

In VLA-SE, the best-fit OPR is 3 within the uncertainties, and in JWST-SE-3 and SE, the best-fit OPR is significantly <3. As shown in Figure 1, these apertures partially overlap, so the conditions sampled by the apertures are not altogether independent. The variations of OPR among the different regions indicate that in some regions (JWST-SE-3 and SE), the ortho → para conversion in the gas (or on grain surfaces) overcomes the OPR-increasing effects of preferential destruction of para-H_2. We will explore this point further below.

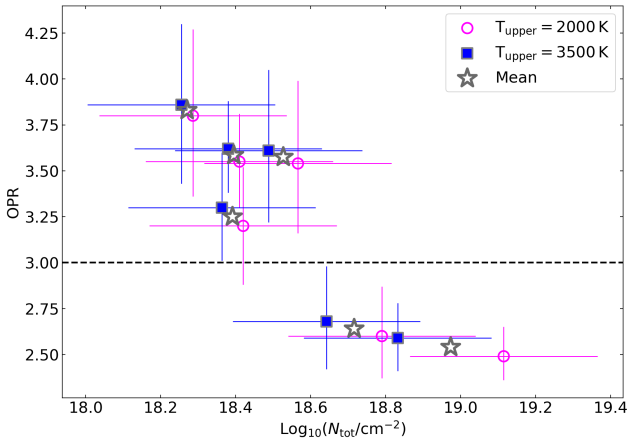

Figure 7. OPR plotted against H_2 column density N_{tot}. The different values of T_u are shown as open (magenta) circles and filled (blue) squares for T_u = 2000 K, 3500 K, respectively. The mean of the two determinations is shown as an open (gray) star. The horizontal dashed line corresponds to the LTE maximum OPR value of 3.

3.5. Non-LTE Excitation of Molecular Hydrogen

To better characterize the warm H_2, we compare the H_2 population diagrams with those predicted by the Meudon PDR models (PDR-7).[25] The UV pumping photophysics in the Meudon model, as well as rate coefficients for collisional excitation and deexcitation of the H_2, should be appropriate for I Zw 18. However, the Meudon PDR models assume dust abundances and coolant (e.g., C^+) abundances appropriate for the Milky Way; thus, applicability of the Meudon models to I Zw 18 is questionable. In addition, the Meudon models assume stationary PDRs, with thermal and chemical balance at each point. The ionization-dissociation fronts in I Zw 18 could be propagating rapidly enough that the stationary approximation may not be valid. Thus, any conclusions drawn from a comparison of I Zw 18 with the models must be regarded as highly tentative.

We first consider isochoric (constant density) models (F. Le Petit et al. 2006; J. Le Bourlot et al. 2012); we varied G_0, the FUV RF intensity, from 10^2 to 10^5 (the maximum value provided in the models), and the H nucleon density, n_H, from 10^2 to 10^6 cm^{-3}. Because of the low extinction in I Zw 18 (Paper I), we limited A_V to a maximum of unity; the viewing angle was taken to be face-on, with inclination = 0°. No fits have been attempted, but we succeed in constraining n_H and G_0.

The results are shown in Figure 8 where only the models that come closest to approximating the observed H_2 are plotted. We find that $G_0/n_H \lesssim 0.05$ cm^3; otherwise the gas is too warm. $G_0 \sim 10^2$ makes the fall-off at low J too steep, since in that case, the gas is too cold. The two best approximations are $G_0 = 10^3$ with either $n_H = 10^5$ cm^{-3}, or $n_H = 10^6$ cm^{-3}. However, $n_H = 10^6$ cm^{-3} (green, orange curves) gives high-J level populations that are too high. Thus, we conclude that $G_0 \sim 10^3$ and $n_H \sim 10^5$ cm^{-3} in the warm H_2 in I Zw 18. These n_H values are toward the upper range of those found in the Orion Bar based on a similar comparison with the Meudon PDR models by E. Peeters et al. (2024).

[25] The Meudon PDR code is part of the ISM database, ISMDB, a web-based fitting tool to fit observations to PDR models https://app.ism.obspm.fr//ismdb/.

We have also compared our H_2 observations with the Meudon isobaric (constant pressure) models; the results are shown in Figure 9. They confirm the G_0 value inferred from the isochoric models, and suggest relatively high pressure; the best approximation to the H_2 population diagrams is a pressure $P/k_B = 5 \times 10^7$ K cm^{-3} (lying roughly between the plotted curves) and $G_0 \sim 10^3$. The high pressures inferred from the PDR models are consistent with those thought to be needed for globular cluster formation ($P/k_B \gtrsim 10^6$ cm^{-3} K, e.g., B. G. Elmegreen & Y. N. Efremov 1997; J. M. D. Kruijssen 2015). In Paper I, we ascribed the nature of the 14 μm continuum sources to young stellar clusters (YSCs), possibly similar to the compact 21 μm-selected sources identified in nearby galaxies by H. Hassani et al. (2023). If JWST-SE-1, 2, and 3 are truly YSCs, then such a high pressure would be necessary to set the stage for their formation. It could also mean that there may be more undiscovered YSCs in I Zw 18, since there is no clear evidence for higher pressure around the continuum sources compared to the other regions.

The values of $G_0 \sim 10^3$ we infer for I Zw 18 are comparable to those found in the N13 PDR in the Small Magellanic Cloud (SMC; I. Y. Clark et al. 2025), although the pressure inferred is roughly six times higher ($P/k_B \sim 5 \times 10^7$ K cm^{-3} versus $P/k_B \sim 8 \times 10^6$ K cm^{-3} for N13 in the SMC). The Meudon PDR models are for gas with $Z \approx Z_\odot$ and dust/gas ratios characteristic of the Milky Way, and are therefore imperfect guides to the PDRs in I Zw 18. The much lower metallicity of I Zw 18 ($Z = 0.03\,Z_\odot$) compared even to the SMC ($Z/Z_\odot \sim 0.2$, L. Toribio San Cipriano et al. 2017) implies reduced rates for dust-catalyzed formation of H_2, reduced photoelectric heating, and reduced cooling by C II and O I. Hence, it would not be surprising if the physical conditions in the PDRs responsible for the H_2 emission in I Zw 18 differ considerably from the Meudon models, and the N31 PDR in the SMC. In Section 4, we discuss the IR emission from dust in four regions of I Zw 18 with strong H_2 emission. The inferred dust temperatures, $T \sim 45$–120 K, likely require $G_0 \sim 10^2$–10^4 to heat the dust, consistent with the G_0 values inferred from the PDR models.

Since the Meudon PDR models include ortho-para conversion (E. Bron et al. 2014, 2016), as well as H_2 photodissociation, we have also compared the Meudon OPR with what we derive from our LTE fits. Over the entire parameter space sampled by the Meudon models, the OPR is <3: in the isochoric, constant-density models, the OPR varies from roughly unity with ($G_0 = 100$, $n_H = 10^4$ cm^{-3}), to roughly 3 with ($G_0 = 10^4$, $n_H = 10^6$ cm^{-3}), and in the isobaric ones, the OPR ranges from 1.5 to 2.7, over P/k_B from 10^6 to 10^8 K cm^{-3}.

As reported in Section 3.4, we find OPR > 3 in three regions, JWST-SE-1, JWST-SE-2, and VLA-NW-A. We speculate that OPR > 3 in I Zw 18 may be a consequence of preferential photodissociation of para-H_2 in a propagating photodissociation front (see Figure 7), with little reformation of H_2 because of the reduced dust abundance.

3.6. Fraction of H_2 in the Apertures

We have estimated the fraction of H_2 falling within the apertures relative to the total H_2 in I Zw 18 by calculating the fraction of the S(1) transition in the extracted spectra with respect to the spectrum extracted from the full Channel 3 cube (see Figure 1). The spectrum extracted from the Channel 3 cube

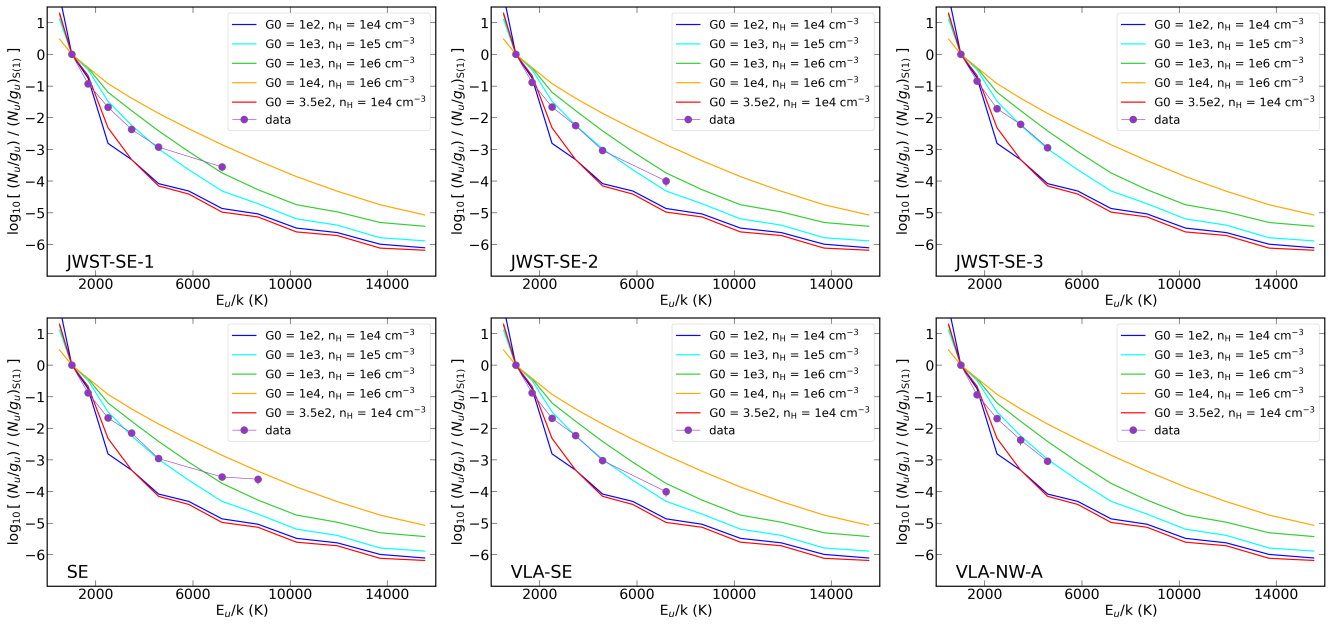

Figure 8. Comparison of I Zw 18 H_2 population diagrams with Meudon PDR-7 isochoric models. The visual extinction A_V was fixed to have a maximum of unity; only the models with $G_0/n_H \leqslant 0.05$ are shown since they best approximate the observed data. Further constraints are discussed in the text.

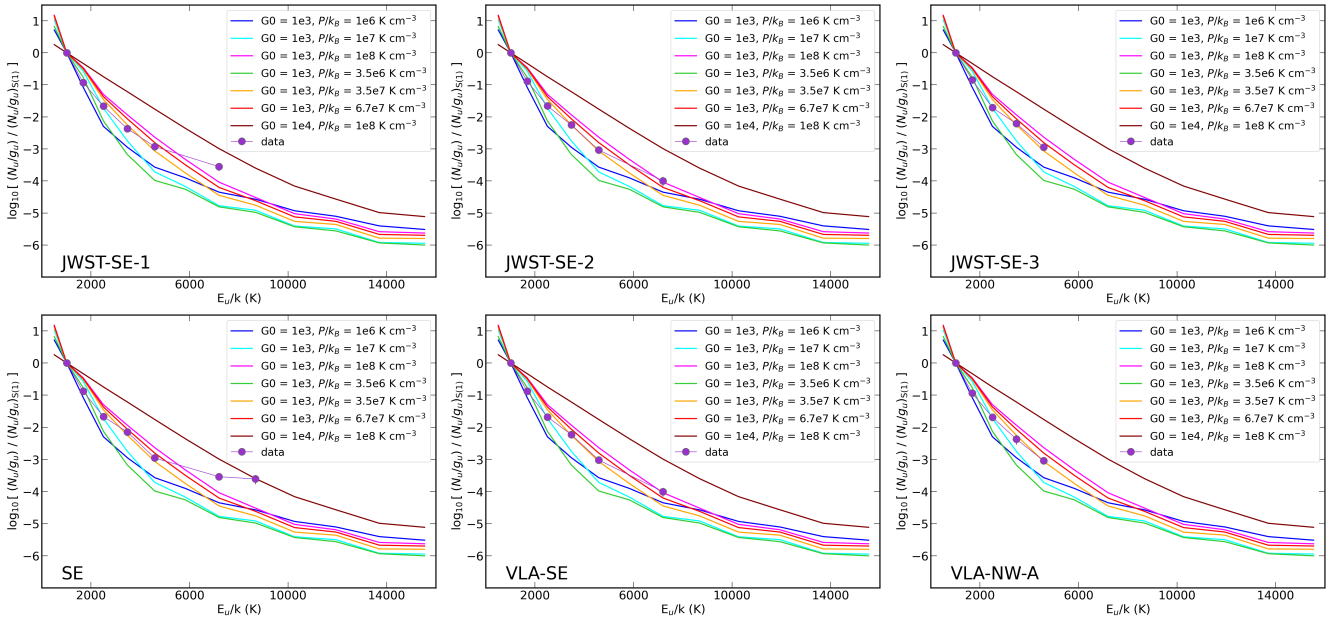

Figure 9. Comparison of I Zw 18 H_2 population diagrams with Meudon PDR-7 isobaric models. As for the isochoric models, the visual extinction A_V was fixed to have a maximum of unity; only the models that best approximate the observed data are shown. Further constraints are discussed in the main text (Section 3.5).

gives an S(1) flux of roughly 2.7×10^{-19} W m^{-2}. The seven independent (non-overlapping) apertures (CO2-1, JWST-SE-1, JWST-SE-2, JWST-SE-3, VLA-NW-A, NW, and VLA-NW-C), together account for $\approx 1.15 \times 10^{-19}$ W m^{-2}, or $\approx 43\%$ of the S(1) flux from the full Channel 3 cube.

The H_2 excitation has been seen to vary among the different apertures, and there may be even greater variation when considering the fainter regions outside the selected apertures. Nevertheless, with $\gtrsim 40\%$ of the S(1) flux, we are likely accounting for an appreciable fraction of the warm H_2 in I Zw 18. Of course, it is possible that there are additional cold H_2 clouds that are not exposed to the heating processes required to populate levels $J_{\rm upper} = 3$ and above.

3.7. Excitation of H_2 and UV Pumping

We have seen that in most regions the observed H_2 $v = 0$ levels in I Zw 18—from $J = 3 \rightarrow 1$ up to $J = 9 \rightarrow 7$—can be reproduced by a simple model with a specified ortho/para ratio OPR, and a specified power-law distribution of temperatures $dN(H_2)/dT \propto T^{-n}$, if the H_2 level populations are assumed to be in LTE at each temperature T. This model predicts that N_i/g_i should depend only on the energy E_i of the excited state, with N_i/g_i monotonically decreasing with increasing E_i.

If the rotationally excited H_2 is due to collisional excitation, we expect vibrationally excited levels to follow the same dependence of N_i/g_i on E_i. However, if UV pumping is important, the vibrationally excited levels will have N_i/g_i

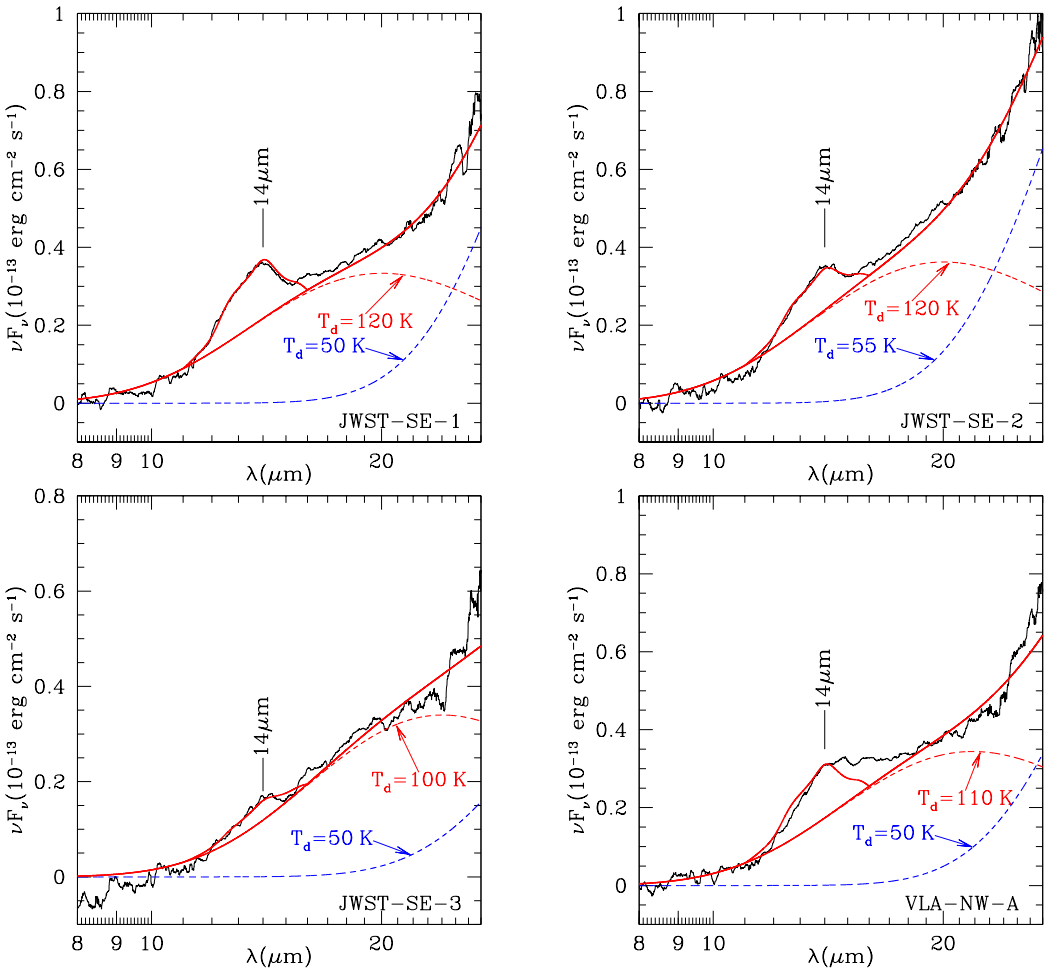

Figure 10. Spectra of dust emission from 8 to 27 μm in JWST-SE-1, JWST-SE-2, JWST-SE-3, and VLA-NW-A. The three SE regions show emission in the broad feature centered near 14 μm (see Figure 11), in addition to a featureless continuum emission. VLA-NW-A appears to have similar emission, but apparently extending to longer wavelengths. The spectra are modeled with two dust temperatures (see Table 4). Dashed curves show the featureless continuum for each of the temperature components.

falling above the trend for the $v = 0$ levels. This behavior is seen in Galactic PDRs (e.g., M. G. Burton et al. 1998; F. Bertoldi et al. 2000; D. M. Meyer et al. 2001). NIRSpec measurements of emission lines from $v = 1$ levels would disclose the role of UV pumping in I Zw 18.

4. Spectral Signature of Dust at Low Metallicity

Here, we focus on the dust continuum apparent in the spectra shown in Figure 2. For this analysis, the data cubes have been convolved to 27 μm resolution prior to the extraction of the spectrum in the selected regions (see Section 2.1). To better reveal the dust continuum emission, the detected emission lines (see Paper I) in the MIRI-MRS spectra have been removed. Then, to improve the S/N, the line-subtracted spectra were smoothed by applying a moving median filter over 71 spectral elements, reducing the effective resolution to $R \approx 60$.

Figure 10 shows the 8–27 μm dust emission for four selected 0.″65 radius regions in Figure 1. These apertures are spatially independent, and correspond to the 14 μm continuum sources introduced in Paper I. The strongest emission is found in the three SE regions, but VLA-NW-A also shows significant emission from the dust continuum. Much of the observed 8–27 μm emission can be reproduced by a power-law opacity $\kappa_c \propto \lambda^{-2}$, and dust temperatures in the range 45–120 K as shown in Figure 10.

4.1. Emission Feature Near 14 μm

In addition to the $\lambda > 10$ μm continuum emission, the four spectra in Figure 10 exhibit an emission feature near ~14 μm. To model the observed feature, we use an empirical profile $F_{\rm obs}(\lambda)$ added to the $\kappa_c \propto \lambda^{-2}$ continuum opacity:

$$\kappa(\lambda) = \kappa_c(13\ \mu\text{m})\left[\left(\frac{13\ \mu\text{m}}{\lambda}\right)^2 + BF_{\rm obs}(\lambda)\right] \qquad (10)$$

The normalized opacity profile $F_{\rm obs}(\lambda)$—peaking near 13 μm—is shown in Figure 11. The overall strength of the profile relative to the continuum is determined by parameter B in Equation (10). The four spectra in Figure 10 are fitted with values of B in the range 0.35–0.8 (see Table 4). Because the opacity peaks near 13 μm, the 14 μm emission feature will also be referred to as the 13 μm opacity feature.

The identity of the 14 μm feature is unknown. Silicates (e.g., $MgSiO_3$ or $Fe_xMg_{2-x}SiO_4$) provide a substantial fraction of the grain mass in the Milky Way, but the absence of an emission feature at 20 μm in the observed spectra (see Figure 10) rules out silicates as a major dust constituent in

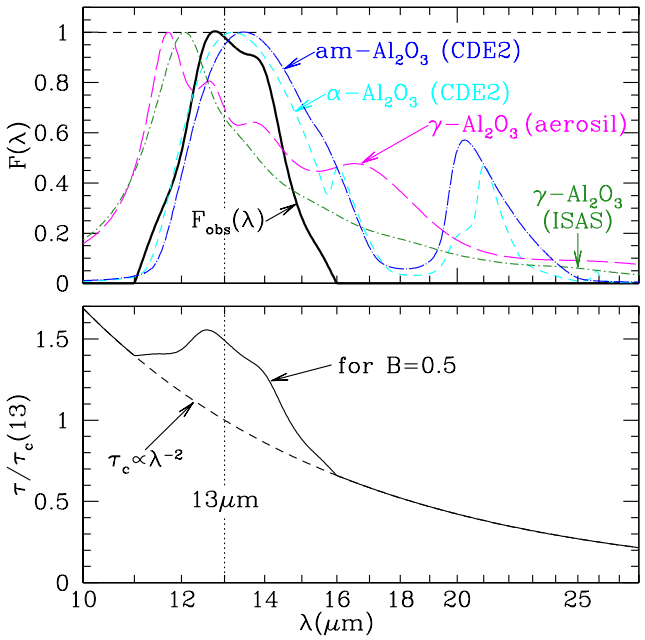

Figure 11. Upper panel: $F_{\rm obs}(\lambda)$ (solid curve) is the normalized opacity profile required to reproduce the observed 14 μm emission feature. Broken curves are opacities either measured or calculated for various samples of Al_2O_3 (see text). Lower panel: model opacity for feature strength parameter $B = 0.5$ (see text and Table 4).

I Zw 18. Iron oxides have infrared features at 17.1 μm for hematite α-Fe_2O_3 (Y. Wang et al. 1998), 15.0 μm for maghemite γ-Fe_2O_3 (B. T. Draine & B. Hensley 2013), and 15.7 μm for magnetite Fe_3O_4 (B. T. Draine & B. Hensley 2013), and ~20–25 μm for wüstite FeO (C. Koike et al. 2017). None of these iron oxides match the I Zw 18 spectra.

In the Milky Way, some dusty outflows from oxygen-rich evolved stars show a "13 μm feature" (T. Posch et al. 1999; G. C. Sloan et al. 2003), but the feature is much narrower (FWHM ≈ 0.55 μm, T. Posch et al. 1999) than the I Zw 18 feature (FWHM ≈ 2.5 μm). Spinel $MgAl_2O_4$ has been suggested (T. Posch et al. 1999; S. Zeidler et al. 2013). Spinels have an accompanying feature at 16.8 μm, which is also present in the spectra of oxygen-rich asymptotic giant branch (AGB) stars. However, there is no evidence of a 16.8 μm feature in the I Zw 18 spectra; hence, spinels seem unlikely to be responsible for the emission in I Zw 18.

Alumina (Al_2O_3) has many crystalline phases. Presolar Al_2O_3 grains, condensed in the outflow from AGB stars, have been found in meteorites (e.g., A. Takigawa et al. 2018). G. C. Sloan et al. (2003) suggest that the 13 μm feature in oxygen-rich evolved stars arises from corundum (α-Al_2O_3). With strong infrared resonances, the opacity of Al_2O_3 particles in the Rayleigh limit is sensitive to particle shape. The opacity calculated for ellipsoids with the "CDE2" distribution of axial ratios (V. Ossenkopf et al. 1992; D. Fabian et al. 2001),[26] using anisotropic optical constants from A. S. Barker (1963), is shown in Figure 11. Also shown is the opacity calculated for ellipsoids with the CDE2 shape distribution, but using optical constants determined for amorphous Al_2O_3 (L. Giacomazzi et al. 2023). α-Al_2O_3 and amorphous Al_2O_3 both have a strong opacity peak near 20 μm that is inconsistent with the I Zw 18 spectra in Figure 10.

Figure 11 also reports measured opacities (C. Koike et al. 1995) for commercially available particles of γ-Al_2O_3 ("aerosil"), as well as for predominantly γ-Al_2O_3 particles produced by combustion of solid rocket fuel ("ISAS"). The γ-Al_2O_3 particles have opacity peaking at 12 μm, inconsistent with I Zw 18. In addition, the "aerosil" particles have a broad absorption peak at ~17 μm, again inconsistent with the I Zw 18 spectra.

Al_2O_3 is predicted to form in SN ejecta (R. Schneider & R. Maiolino 2024). However, none of the Al_2O_3 variants considered provide a good match to the observed spectra. α-Al_2O_3 and amorphous Al_2O_3 both have a strong peak near 13 μm, but are ruled out by a secondary peak near 20 μm that is absent in the observed spectra. Samples of predominantly γ-Al_2O_3 (the "aerosil" and "ISAS" curves in Figure 11) lack the 20 μm feature, but do not provide a good match to $F_{\rm obs}$. Because silicates, iron oxides, and spinels appear to be inconsistent with the observed spectra, we seek another refractory material composed of reasonably abundant elements to provide the broad 13 μm opacity peak needed to explain the 14 μm emission feature. While none of the examples of Al_2O_3 studied provide a good match to the observed spectral shape, all forms of Al_2O_3 exhibit strong absorption somewhere in the 12–15 μm range, with dielectric functions that make the opacity profile quite sensitive to particle shape. Some forms of Al_2O_3 (e.g., "ISAS" γ-Al_2O_3) lack strong emission features near 20 μm. We tentatively identify the 14 μm feature as being dust to some form of Al_2O_3-based material.

The spectrum of VLA-NW-A also appears to show a possible emission excess on the red shoulder of the 14 μm emission feature (see Figure 10). If real (i.e., not due to noise or inaccurate background subtraction), this implies either a change in the profile of the 14μm feature, or an additional emission component at ~15 μm.

4.2. Dust Mass

A $\kappa_c \propto \lambda^{-2}$ opacity could plausibly arise from metallic grains or amorphous carbon grains. Iron grains were proposed to explain the featureless mid-infrared emission from the winds from low-metallicity AGB stars in globular clusters (I. McDonald et al. 2010, 2011). For purposes of estimating the mass of the continuum-emitting dust, we adopt a provisional opacity $\kappa_c(13\ \mu{\rm m}) = 1 \times 10^3\ {\rm cm^2\,g^{-1}}$. This is much larger than estimates for the opacity of metallic Fe grains,[27] but is comparable to estimates for, say, amorphous carbon (F. Rouleau & P. G. Martin 1991; V. G. Zubko et al. 1996; C. Jäger et al. 1998).

The 10–27 μm spectra in Figure 10 require at least two dust temperatures; "hot" dust with $T \approx 100$ K, and "warm" dust with $T \approx 50$ K. Masses of the hot and warm dust components are given in Table 4. The bulk of the dust mass is in the lower temperature component. Dust masses are for the provisional opacity $\kappa_c = 1 \times 10^3 (13\ \mu{\rm m}/\lambda)^{-2}\ {\rm cm^2\,g^{-1}}$; if the actual opacity is higher or lower, the dust masses will be lower or higher.

[26] We assume that the α-Al_2O_3 c-axis is equally likely to be parallel to any of the principal axes of the ellipsoids.

[27] $a = 0.01$ μm spheres composed of bcc Fe have $\kappa(\lambda) \approx 12(\lambda/10\ \mu{\rm m})^{-2}$ ${\rm cm^2\,g^{-1}}$ at $T = 300$K (B. T. Draine & B. Hensley 2013, Appendix B), with κ decreasing as T is decreased. However, if the electron scattering time is greatly decreased by impurities (e.g., Ni, Mg, Al, C, O) or defects, the opacity could be substantially increased. Our provisional opacity $\kappa_c = 10^3(\lambda/13\ \mu{\rm m})^{-2}$ should be regarded as very uncertain.

Table 4
Dust Properties in Selected Regions

Region	B[a]	$T_{d,\rm hot}$ (K)	$T_{d,\rm warm}$ (K)	$M_{d,\rm hot}$[b] ($M_\odot$)	$M_{d,\rm warm}$[b] ($M_\odot$)	$M_{\rm HI}$ ($M_\odot$)	$M_d/M_{\rm H\,I}$	$f_{\rm dust}$
JWST-SE-1	0.7	120	50	0.07	59	7.1×10^5	8×10^{-5}	0.3
JWST-SE-2	0.45	120	55	0.07	32	7.6×10^5	4×10^{-5}	0.14
JWST-SE-3	0.35	100	50	0.20	20	9.9×10^5	2×10^{-5}	0.07
VLA-NW-A	0.8	110	50	0.12	44	2.0×10^5	2×10^{-4}	0.7

Notes.
[a] Parameter in Equation (10) determining strength of the 13.5μm feature.
[b] Assuming $\kappa_c(\lambda) = 10^3\ {\rm cm^2 g^{-1}} (\lambda/13\ \mu{\rm m})^{-2}$, and $D = 18.2$ Mpc.

We have estimated the H I mass $M_{\rm H\,I}$ in the JWST-SE-1, JWST-SE-2, JWST-SE-3, and VLA-NW-A apertures using $N_{\rm H\,I}$ from the 2″ resolution HI map of F. Lelli et al. (2012); the values are given in Table 4. The corresponding $N_{\rm HI}$ column densities range from $2 \times 10^{21}\ {\rm cm^{-2}}$ in VLA-NW-A to $\sim 10^{22}\ {\rm cm^{-2}}$ in the SE apertures. The ratio of refractory grain mass to H mass $M_d/M_{\rm H} = f_{\rm dust} \times 0.01 (Z/Z_\odot) = 3 \times 10^{-4} f_{\rm dust}$, where $f_{\rm dust} < 1$ is the fraction of the refractory elements that are contained in the dust, and 0.01 corresponds to the assumed value of the dust-to-H nucleon mass ratio at Solar metallicity (G. Aniano et al. 2020). For the dust mass estimates in Table 4, $f_{\rm dust}$ ranges from 0.07 in JWST-SE-3 to 0.7 in VLA-NW-A. While the Milky Way has $f_{\rm dust} \approx 1$, low-metallicity galaxies are usually found to have low global values of $f_{\rm dust}$, with $f_{\rm dust} \lesssim 0.01$ for $Z/Z_\odot \lesssim 0.05$ (e.g., A. Rémy-Ruyer et al. 2014). However, in galaxies with metallicities as low as $Z/Z_\odot \sim 0.1$, regions of high HI column density $\sim 10^{22}\ {\rm cm^{-2}}$ can have $f_{\rm dust} \lesssim 1$ (A. Hamanowicz et al. 2024). It is therefore perhaps not surprising to find $f_{\rm dust}$ as large as 0.3 and 0.7 in JWST-SE-1 and VLA-NW-A.

Because our spectroscopy stops at $\sim 27\ \mu$m, the JWST observations are insensitive to cooler dust. Using photometry from Spitzer and Herschel, D. B. Fisher et al. (2014) estimated a total dust mass $M_{\rm dust} \approx 900^{+900}_{-500}\ M_\odot$, while L. K. Hunt et al. (2014) estimated $M_{\rm dust} \approx 340 \pm 10\ M_\odot$. Our similar estimate here from only a limited area arises from use of a lower (but uncertain) opacity for metallic grains at $\sim 25\ \mu$m. While VLA-NW-A is much less bright at 11.3 μm than JWST-SE-1 and JWST-SE-2 (see Figure 1), the dust mass seems to be comparable in the three sources; the 11.3 μm emission is weak only because the "hot" dust is slightly cooler than in JWST-SE-1 and JWST-SE-2.

The opacity of the material responsible for the 14 μm emission feature is unknown. Crystalline α-Al_2O_3 and amorphous Al_2O_3 particles with the CDE2 shape distribution have $\kappa(13\ \mu{\rm m}) \approx 7300$ and $8200\ {\rm cm^2\ g^{-1}}$, respectively. For $\kappa(13\ \mu{\rm m}) \approx 8000\ {\rm cm^2\ g^{-1}}$, the mass of Al_2O_3 material is

$$M_{\rm Al_2O_3} \approx B \frac{\kappa_c(13\mu{\rm m})}{\kappa_{\rm Al_2O_3}(13\mu{\rm m})} M_c \approx \frac{B}{8} M_c. \quad (11)$$

where M_c is the mass of the material responsible for the continuum emission (assuming $\kappa_c(13\ \mu{\rm m}) \approx 10^3\ {\rm cm^2\ g^{-1}}$). With $B \approx 0.5$, the Al_2O_3 would account for only $\sim$7% of the total dust mass.

It seems likely that dust chemistry in low-metallicity galaxies at high redshifts will resemble what is happening in I Zw 18: injection of elements from evolved stars and supernovae into a nearly dustless ISM permeated with harsh ultraviolet radiation, heating the interstellar dust to $T \gtrsim 50$ K. Dust formed in the stellar outflows will undergo both growth and destruction in the ISM. The end-product present in I Zw 18 —metallic or carbonaceous material plus an unidentified compound (possibly Al_2O_3) producing the broad emission feature near 14 μm—may be a guide to dust physics in young galaxies at $z > 10$.

4.3. Searching for PAH Emission in I Zw 18

It is well known that in metal-poor environments, PAH emission tends to be suppressed (e.g., C. W. Engelbracht et al. 2005; S. C. Madden et al. 2006; L. K. Hunt et al. 2010). Nevertheless, given the high S/N of our MIRI spectra of I Zw 18, we have looked for PAHs by comparing I Zw 18 to the templates of the Orion Bar from PDRs4All (R. Chown et al. 2024). During the line search described in Section 2.2, we used the wavelengths given in R. Chown et al. (2024) as initial guesses for PAH features; only one, in JWST-SE-1 at $\sim 11\ \mu$m, has S/N $\gtrsim 5$.

Because we would expect PAH emission together with H_2 in PDRs, to increase S/N, we have averaged the spectra in the five regions to the SE in I Zw 18, where we find most of the H_2. Figure 12 shows this mean SE spectrum compared to the PDRs4All Orion Bar templates by R. Chown et al. (2024). The latter have been normalized to the I Zw 18 spectra at $\sim 10.9\ \mu$m. The left panel illustrates the entire MIRI spectral range, while the middle panel zooms in around $\sim 7\ \mu$m; the right panel shows a close-up around the 11.2 μm PAH feature, thought to be a carrier of large, neutral PAHs (e.g., B. T. Draine et al. 2021; D. Rigopoulou et al. 2021). Because the apertures are not independent (see Figure 1), this is not a rigorous exercise; the aim is a qualitative enhancement of any PAH emission features.

It can be seen from Figure 12 that I Zw 18 does not resemble a typical metal-rich H II region or PDR. Although the continuum of the stacked SE spectrum in the left panel rises toward the red, most similar to the Orion Bar H II region, it also has a significant bump at $\sim 14\ \mu$m (see Section 4.1). Even with the stacks, the S/N between 6 and 7 μm in the middle panel is insufficient to characterize PAH features with any certainty, although there is an enhancement in I Zw 18 around $\sim$5.8–6.0 μm, blueward of where a PAH feature is seen in the Orion spectra. The right panel of Figure 12 shows an enhancement around 11.25 μm, but we hesitate to consider this a true detection of the nanoparticles associated with PAHs or other aromatic features. If these are PAHs, they are radically different from any such emission previously known.

There is no measurable PAH emission at 7.7 μm in I Zw 18. Previous work has shown that in low-metallicity dwarfs, like in more metal-enriched galaxies, the 7.7 μm feature tends to

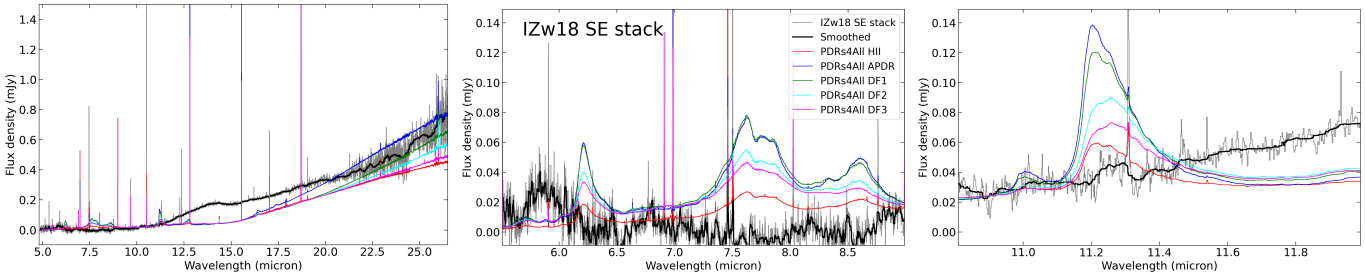

Figure 12. I Zw 18 stacked spectra from the SE compared with templates from PDRs4All (R. Chown et al. 2024). The left panel shows the full wavelength coverage; the middle panels show a zoom-in around ∼7 μm, and the right around 11 μm. PDR templates are normalized in all panels to the mean at 10.9 μm; all flux density units are mJy for I Zw 18, and for the PDRs are arbitrary, rescaled to the normalization. The PDRs4All templates are given by colored curves as in the legend, and the I Zw 18 stacked spectrum is in gray, with the smoothed data as heavy black curves. It can be seen that the I Zw 18 spectra have a "bump" at ∼14 μm, implying warmer dust than the PDRs4All Orion Bar templates with possibly a different dust composition. Moreover, there is no discernible PAH emission between 5 and 8 μm, nor clearly at ∼ 11.2 μm.

dominate the total PAH emission carried by each band (e.g., L. K. Hunt et al. 2010; K. M. Sandstrom et al. 2012; J. Chastenet et al. 2019). However, the ratio of 7.7 μm intensity, relative to warm dust grain emission, is suppressed at low metallicity (R. Chown et al. 2025). PAH emission in metal-poor environments also tends to be preferentially lost in ionized gas relative to the diffuse neutral medium, even at comparable RF intensities (e.g., J. Chastenet et al. 2019). Since the apertures we have used for this analysis of I Zw 18 are either directly associated with HII regions or contain copious quantities of ionized gas (see Paper I), this could be part of the reason for the lack of discernible PAH emission in the MIRI spectra.

Indeed, the lack of PAH emission could be because the PAH particles are destroyed by the strong RF, capable of exciting [O IV] and [Ne V], or it could be because they are unable to form in the first place given the paucity of dust. If only very small PAHs are present, the strongest PAH emission feature might be the 3.3 μm C–H stretch (e.g., B. T. Draine et al. 2021; D. Rigopoulou et al. 2021). This feature is associated with neutral PAHs, which may be more robust than ionized PAHs under extreme conditions (e.g., I. García-Bernete et al. 2024; D. Rigopoulou et al. 2024). NIRSpec data would be needed to search for this feature. While the lack of PAH emission is not particularly surprising, the MIRI spectra of I Zw 18 supply strong constraints for dust models at these low metallicities.

5. Discussion

Despite the low dust content in I Zw 18 (D. B. Fisher et al. 2014; L. K. Hunt et al. 2014), there is measurable warm H_2, in particular in the SE, where all five of the aperture spectra have significant H_2 detections in at least five transitions (see Table 3). The warm H_2 column densities are more than one order of magnitude below the typical values in more massive spirals. The warm H_2 masses we measure within 120 pc diameter regions range from $\sim 300\,M_\odot$ to $\sim 2000\,M_\odot$, again roughly an order of magnitude lower than the virial H_2 cloud masses found by M. Rubio et al. (2015) and Y. Shi et al. (2020) from CO measured in galaxies with metallicities around 7%–13% $Z_\odot$ (WLM, Sextans B). As mentioned above, T_l is well constrained by our fits, so that we may be detecting most of the total H_2 content with the rotational lines. The heating (from UV pumping of H_2, plus photoelectrons from the grains that are present, some heating by X-rays, and presumably cosmic rays) may be able to maintain the warm H_2 (i.e., $T_l \gtrsim 150$ K), even in gas that is self-shielded by $N_{\rm tot} \approx 10^{18}$ cm^{-2}. It is likely that the H_2 was cooler before the starburst, but once OB stars turned on, the FUV may be sufficient to keep the H_2 warm.

An OPR in the $v = 0$ H_2 levels of >3 is measured in three independent regions. We attribute this to more rapid photodissociation of H_2, relative to its formation rate, which results in more effective self-shielding in ortho-H_2 with respect to its para counterpart. This raises the OPR above its LTE value; if photodissociation is sufficiently rapid compared to the rates for ortho-para conversion in the gas (or on grain surfaces), selective photodissociation will result in OPR > 3. Because the photodissociation rate rises as H_2 column density $N_{\rm tot}$ decreases, this is consistent with the observed trend in Figure 7 for OPR to be higher in regions of lower $N_{\rm tot}$.

If we are truly detecting most of the H_2 in I Zw 18 with MIRI, then we are faced with the question of whether or not stars can form from this warm gas. The answer to this is not clear. Given the lack of cool H_2, it could be that star formation is occurring in reservoirs of atomic gas as proposed by S. C. O. Glover & P. C. Clark (2012) and M. R. Krumholz (2012). However, because the lowest-J H_2 transition is not covered by our observations, they are insensitive to the coolest component of H_2 with temperatures $\lesssim$100 K; possibly we are detecting just the tip of the iceberg of the total H_2 mass as the potential fuel for future star formation in I Zw 18.

The detection of H_2 up to $J_{\rm upper} = 10$ (Table 3) raises the question of gas density. The comparison of the H_2 population diagrams in I Zw 18 with the isochoric Meudon PDR models indicates molecular-gas densities of $\sim 10^5$ cm^{-3}, at least for the higher-J transitions. Optical and radio observations of the ionized gas in I Zw 18 (Y. I. Izotov et al. 1999; L. K. Hunt et al. 2005) suggest that the electron density is fairly low, $\lesssim$100 cm^{-3} (see also Paper III). The implication is that within 120 pc regions in I Zw 18 there is neutral warm, dense gas at ∼200 K coexisting with highly ionized, more tenuous, gas at ∼20,000 K. The highest ionized gas densities will be near ionization fronts. If some of these have $n_e \gtrsim 2500$ cm^{-3} and $T \approx 20{,}000$ K (e.g., Paper III), and the ionization front has evolved to become D-type, the PDR will have a similar pressure $p/k_{\rm B} \approx 10^8$ K cm^{-3}. The zone in the PDR where $T \approx 10^3$ K would then have $n \approx 10^5$ cm^{-3}, sufficient to approximately thermalize the high-J levels.

Possibly the most complex aspect of our results is that highly ionized gas such as [O IV] and [Ne V] found in several of the apertures considered here (Paper I) can coexist with warm H_2 within the same 120 pc region. We would naively expect

that the strong RF that excites the gas would photodissociate H_2. However, there could be a "sweet spot" such that the dense, neutral gas emitting H_2 lives in an environment that is warm, self-shielded from FUV, but not sufficiently hot to collisionally dissociate the molecule (a similar argument for vibrationally excited H_2 can be found in B. T. Draine & D. T. Woods 1990). Some of the radiation from the sources responsible for the observed [Ne v] (which requires $h\nu > 97$ eV) may penetrate into and provide heating of the partially ionized molecular gas.

That molecular clouds can survive in extreme conditions is shown by the observations of M. T. Valdivia-Mena et al. (2025), who find subparsec and parsec-sized clumps of dense molecular gas around the young massive cluster R136, in the Large Magellanic Cloud. R136 is a 1−2 Myr old compact star cluster hosting several stars more massive than 150 $M_\odot$ (P. A. Crowther et al. 2010). The molecular clumps lie within 2 and 10 pc in projection from R136, appearing to be the densest remnants of the molecular reservoir that has been carved out through intense radiation.

6. Summary

In order to characterize the ISM in an extreme, metal-poor dwarf galaxy, we obtained JWST MIRI/MRS observations of the main body of I Zw 18. Spectra have been extracted from the convolved cubes within 11 apertures (Figure 1), each ∼120 pc in diameter, placed on regions of interest across the galaxy (Figure 2). Here we have focused on the analysis of H_2 and the dust continuum, and our findings can be summarized as follows:

1. MIRI has detected a series of rotational H_2 lines from S(1) to S(8) (S(0) is beyond the sensitivity range of MIRI). We fit population diagrams in six of the eleven apertures with five or more significant H_2 detections (Figures 3, 4), assuming a continuous temperature distribution. The best-fit power-law index for the temperature distribution tends to be flatter than for more massive spirals, implying an excess of warm H_2 gas. Interestingly, while H_2 emission is seen, our criterion of 5 or more significant H_2 detections was not met in the aperture centered on the CO(2–1) detection.
2. In a second series of fits, we left the H_2 OPR as a free parameter and found OPR significantly > 3 in three of the six apertures for which we were able to construct population diagrams (Figures 3, 5). Although OPR > 3 in PDRs has been considered a theoretical possibility (e.g., B. T. Draine & F. Bertoldi 1996; A. Sternberg & D. A. Neufeld 1999), it has never before been measured in interstellar gas.
3. Comparing the emission measured in different (sometimes overlapping) apertures, we find (Figure 7) that OPR tends to increase with decreasing H_2 column density, $N_{\rm tot}$, consistent with OPR > 3 resulting from selective photodissociation.
4. Comparison of the H_2 population diagrams with Meudon PDR isochoric and isobaric models suggests a $G_0/n_{\rm H}$ ratio $\lesssim 0.05$ cm^3 and a H nucleon density of $\sim 10^5$ cm^{-3} (Figures 8, 9). This dense gas coexists within the same ∼120 pc region as highly ionized, more tenuous, gas emitting [O IV] and [Ne v]. These different gas phases appear to be in approximate pressure equilibrium. Nevertheless, the comparison with the Meudon PDR models must be interpreted with caution because of the extreme physical conditions in I Zw 18 not accounted for in the models.
5. An unidentified dust emission feature at ∼14 μm was found in I Zw 18's continuum spectra in three regions in the SE, and in VLA-NW-A (Figure 10). Silicates, iron oxides, and spinels appear unable to account for the observed feature. The feature may be due to alumina (Al_2O_3), predicted to be found in dust produced by supernovae (e.g., S. Marassi et al. 2019; R. Schneider & R. Maiolino 2024), and in outflows from O-rich AGB stars (F. Dell'Agli et al. 2014; A. Takigawa et al. 2018). All forms of Al_2O_3 have strong absorption near 13 μm, but the 10–20 μm spectrum varies considerably from one sample to another. While none of the Al_2O_3 compositions studied here provides a good match to the observed spectra, we tentatively identify the 14 μm emission in I Zw 18 as being due to some form of Al_2O_3.
6. The dust-to-gas mass ratio in these four regions indicates that a substantial fraction, from ∼0.1 to 0.7, of the refractory elements is incorporated in dust grains, although this result is sensitive to the adopted grain opacity.
7. We searched for PAH emission in I Zw 18 by comparing templates from PDRs4ALL (Figure 12). There is little evidence for PAH emission in I Zw 18, at least at MIRI wavelengths, although stacking the SE spectra hints at a very weak, tentative 11.2 μm feature.

Warm H_2 emission in one transition, S(1), was also recently found in another dwarf galaxy at a similar low metallicity, Leo P (O. G. Telford et al. 2024), powered by a single O star (C. J. Evans et al. 2019). Now in I Zw 18, a dwarf starburst also at 3% Solar metal abundance, we have been able to fit H_2 level population diagrams and derive H_2 column densities, parameters of continuous temperature distributions, and even infer the OPR. The H_2 gas in I Zw 18 is warm, so it is not clear whether stars can form from the H_2 we measure here. Nevertheless, the presence of H_2 even at these low levels of chemical enrichment casts doubt on the need to form stars in pure atomic gas in these extreme environments (e.g., S. C. O. Glover & P. C. Clark 2012; M. R. Krumholz 2012). The constraints provided by our observations on H_2 formation and destruction in a chemically unevolved ISM will help to better model the metal-poor dwarf galaxy population being identified by JWST at high redshift.

Acknowledgments

We are grateful to the anonymous referee for comments that helped improve the paper. We warmly thank Federico Lelli for the H I zero-moment map taken from F. Lelli et al. (2012). This work is based on observations made with the NASA/ESA/CSA James Webb Space Telescope. The data were obtained from the Mikulski Archive for Space Telescopes at the Space Telescope Science Institute, which is operated by the Association of Universities for Research in Astronomy, Inc., under NASA contract NAS 5-03127 for JWST. These observations are associated with program JWST-3533, under JWST grant No. B0227. R.R.V. is grateful for the support of this program, provided by NASA through a grant from the Space Telescope Science Institute. S.H., B.L.J., and

M. Mingozzi are thankful for support from the European Space Agency (ESA). M. Meixner acknowledges that a portion of her research was carried out at the Jet Propulsion Laboratory, California Institute of Technology, under a contract with the National Aeronautics and Space Administration (80NM0018D0004). B.T.D. thanks Greg Sloan for very helpful discussions. L.K.H. gratefully acknowledges Martha Haynes for interesting exchanges, her patience, and for sharing her understanding of low-metallicity galaxies.

Facilities: JWST (MIRI), HST (ACS), Keck (KCWI).

Software: Astropy (Astropy Collaboration et al. 2013, 2018), Numpy (C. R. Harris et al. 2020), SciPy (P. Virtanen et al. 2020), dustmaps (G. Green 2018), emcee (D. Foreman-Mackey et al. 2013).

The JWST data presented in this article were obtained from the Mikulski Archive for Space Telescopes (MAST) at the Space Telescope Science Institute. The specific observations analyzed can be accessed via Doi: 10.17909/n80x-b534.

Appendix A
Flux Measurements of Detected H_2 Lines in the 1D Spectra from the Convolved Cubes

Figure 13 shows the fits for the rotational H_2 lines seen in a representative region, JWST-SE-2, and Tables 5 and 6 report the measured fluxes for all apertures within a radius of 0."65 as described in Section 2.2.

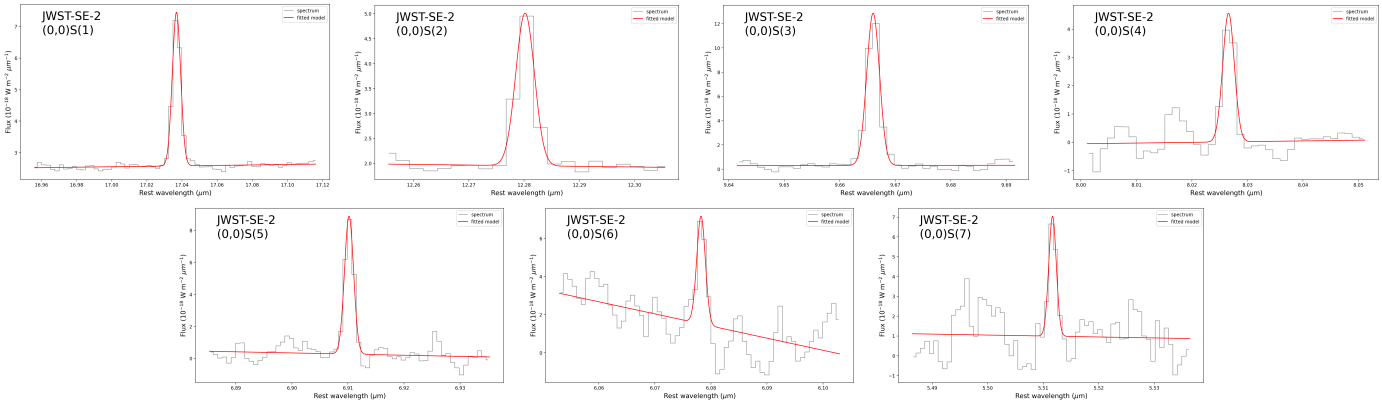

Figure 13. Gaussian line fits to the detected H_2 lines in a representative region, JWST-SE-2; the vertical flux density scale is in units of 10^{-18} W m^{-2} μm. More details are given in the main text.

Table 5
Integrated Line Fluxes from the Convolved Cubes in the NW-region 1.″3 Diameter Apertures with S/N $\geqslant$ 3

Line	Rest λ (μm)	NW	VLA-NW-A	VLA-NW-B	VLA-NW-C	CO2-1	ULX-1
				(10^{-21} W m^{-2})			
H_2 lines							
(0,0)S(1)	17.0348	2.78 ± 0.60	19.64 ± 0.49	⋯	4.07 ± 0.99	2.53 ± 0.51	⋯
(0,0)S(2)	12.2786	⋯	7.81 ± 0.71	⋯	⋯	⋯	⋯
(0,0)S(3)	9.6649	4.00 ± 1.14	23.05 ± 1.21	⋯	14.48 ± 2.89	5.50 ± 1.46	⋯
(0,0)S(4)	8.0251	⋯	6.13 ± 2.02	⋯	⋯	⋯	⋯
(0,0)S(5)	6.9095	⋯	11.64 ± 1.66	⋯	⋯	⋯	⋯
(0,0)S(7)	5.5112	35.32 ± 6.97	⋯	⋯	⋯	⋯	13.32 ± 3.63
(0,0)S(8)	5.053	27.21 ± 6.84	⋯	⋯	⋯	16.27 ± 4.62	19.58 ± 3.90

Table 6
Integrated Line Fluxes from the Convolved Cubes in the SE-region 1.″3 Diameter Apertures with S/N $\geqslant$ 3

Line	Rest λ (μm)	JWST-SE-1	JWST-SE-2	JWST-SE-3	SE	VLA-SE
				(10^{-21} W m^{-2})		
H_2 lines						
(0,0)S(1)	17.0348	25.47 ± 0.70	28.93 ± 0.73	31.38 ± 0.75	27.73 ± 0.77	23.27 ± 0.70
(0,0)S(2)	12.2786	10.35 ± 1.08	12.94 ± 0.65	15.51 ± 0.74	12.65 ± 1.23	10.57 ± 0.74
(0,0)S(3)	9.6649	31.47 ± 1.45	36.38 ± 1.61	34.83 ± 1.21	33.88 ± 1.60	27.84 ± 1.43
(0,0)S(4)	8.0251	7.94 ± 1.79	11.87 ± 2.30	14.11 ± 1.64	14.41 ± 1.61	10.08 ± 1.87
(0,0)S(5)	6.9095	19.68 ± 1.60	17.44 ± 1.64	23.26 ± 1.18	20.04 ± 1.07	14.54 ± 1.28
(0,0)S(7)	5.5112	25.12 ± 6.96	10.29 ± 3.38	⋯	28.25 ± 6.07	8.13 ± 2.51
(0,0)S(8)	5.053	⋯	⋯	⋯	15.65 ± 4.97	⋯

Appendix B
Comparison of the H_2 Population Diagram Fits with $T_u = 2000$ K and $T_u = 3500$ K

We have also fit the H_2 population diagrams with $T_u = 3500$ K, and find very similar results. Table 7 gives the best-fit values, analogous to Table 3, and Figure 14 compares, for the two T_u values, the best-fit T_l and the power-law index n. The similarities of the H_2 column densities and masses within the apertures, as well as the OPR, are discussed in the main text.

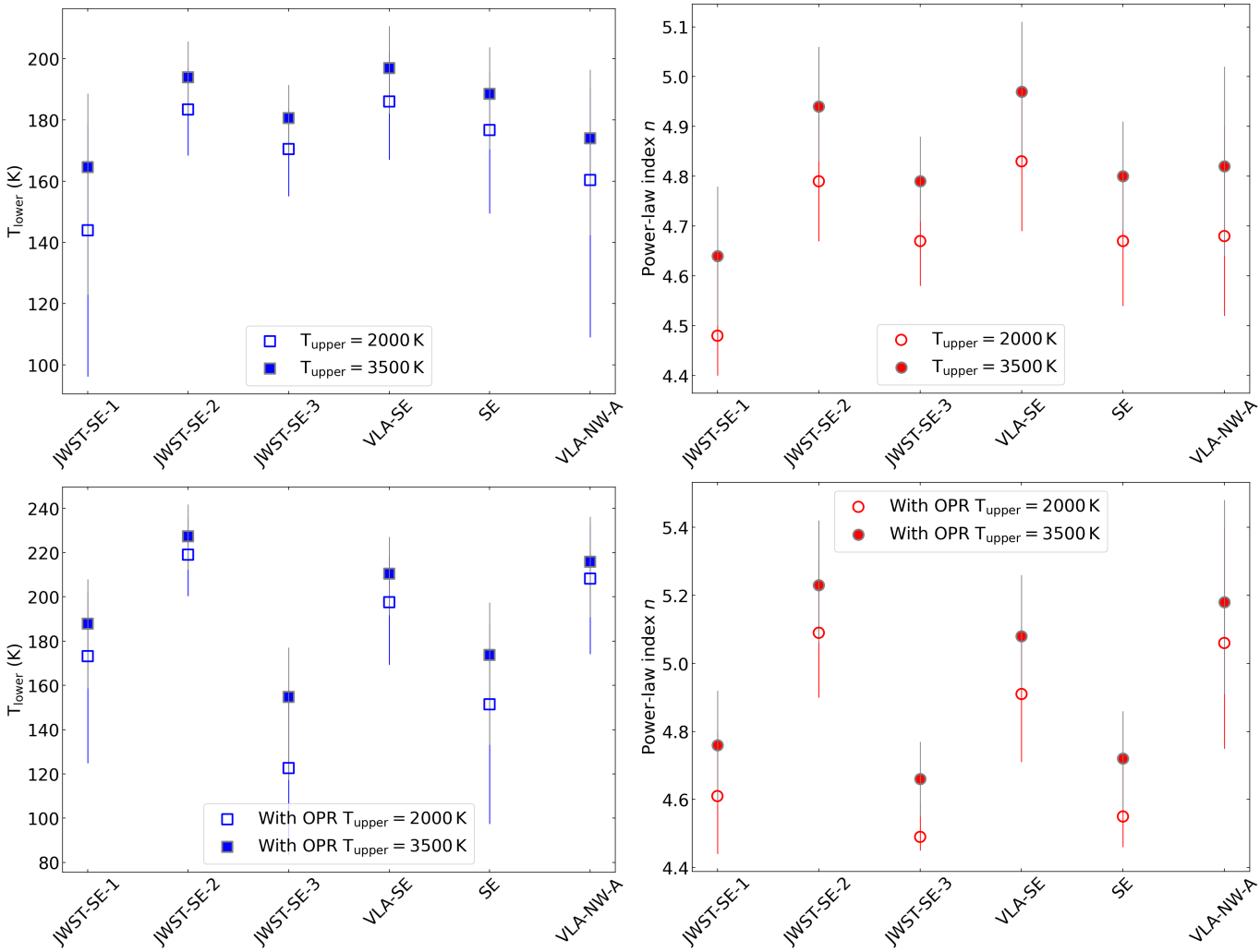

Figure 14. Comparison of the H_2 population diagram best-fit parameters with $T_u = 2000$ K and $T_u = 3500$ K. The lower panels including "With OPR" in the legends correspond to the 3-parameter fits, and the upper ones to the 2-parameter fits with OPR = 3. Filled symbols correspond to $T_u = 3500$ K, and open ones to $T_u = 3500$ K. T_l comparisons are shown by blue squares, and n by red circles.

Table 7
Best-fit Results for H_2 Population Diagrams with $T_u = 3500$ K

Region	Number points	Max J_{low}	T_l (K)	n	OPR	$\log_{10}(N_{tot}/cm^{-2})$[a]	$\log_{10}(H_2/M_\odot)$[b]	AIC[c]	BIC[d]	χ^2
(1)	(2)	(3)	(4)	(5)	(6)	(7)	(8)	(9)	(10)	(11)
OPR = 3										
JWST-SE-1	6	7	165^{+42}_{-24}	$4.64^{+0.14}_{-0.14}$	⋯	18.65 ± 0.35	2.86 ± 0.35	4.69	4.28	6.74
JWST-SE-2	6	7	194^{+12}_{-12}	$4.94^{+0.11}_{-0.12}$	⋯	18.54 ± 0.06	2.76 ± 0.06	7.54	7.12	10.82
JWST-SE-3	5	5	181^{+12}_{-11}	$4.79^{+0.08}_{-0.09}$	⋯	18.65 ± 0.07	2.86 ± 0.07	6.00	5.22	7.45
SE	7	8	189^{+18}_{-15}	$4.80^{+0.11}_{-0.11}$	⋯	18.54 ± 0.12	2.76 ± 0.12	12.83	12.73	24.73
VLA-SE	6	7	197^{+15}_{-14}	$4.97^{+0.13}_{-0.14}$	⋯	18.44 ± 0.09	2.65 ± 0.09	3.05	2.63	5.12
VLA-NW-A	5	5	174^{+32}_{-22}	$4.82^{+0.18}_{-0.20}$	⋯	18.49 ± 0.26	2.71 ± 0.26	4.70	3.92	5.75
Fitting OPR										
JWST-SE-1	6	7	188^{+29}_{-20}	$4.76^{+0.17}_{-0.16}$	$3.61^{+0.39}_{-0.44}$	18.49 ± 0.22	2.71 ± 0.22	3.15	2.52	3.73
JWST-SE-2	6	7	227^{+15}_{-14}	$5.23^{+0.17}_{-0.19}$	$3.62^{+0.24}_{-0.26}$	18.38 ± 0.06	2.60 ± 0.06	3.64	3.01	4.05
JWST-SE-3	5	5	155^{+38}_{-22}	$4.66^{+0.11}_{-0.11}$	$2.59^{+0.18}_{-0.19}$	18.83 ± 0.27	3.05 ± 0.27	3.01	1.84	2.75
SE	7	8	174^{+41}_{-24}	$4.72^{+0.15}_{-0.14}$	$2.68^{+0.26}_{-0.30}$	18.64 ± 0.35	2.86 ± 0.35	14.48	14.31	23.49
VLA-SE	6	7	$210^{+19}_{-16.7}$	$5.08^{+0.16}_{-0.18}$	$3.30^{+0.29}_{-0.30}$	18.36 ± 0.10	2.58 ± 0.10	3.58	2.95	4.01
VLA-NW-A	5	5	216^{+25}_{-20}	$5.18^{+0.27}_{-0.30}$	$3.86^{+0.43}_{-0.44}$	18.26 ± 0.11	2.47 ± 0.11	–4.02	–5.19	0.67

Notes.
[a] Calculated from Equation (8).
[b] Calculated from Equation (9).
[c] Calculated according to `SciPy/optimize`: AIC $= N \ln(\chi^2/N) + 2N_{fit}$ where N_{fit} is the number of fitted parameters, and N is the number of data points.
[d] Calculated according to `SciPy/optimize`: BIC $= N \ln(\chi^2/N) + \ln(N)N_{fit}$.

ORCID iDs

L. K. Hunt https://orcid.org/0000-0001-9162-2371
B. T. Draine https://orcid.org/0000-0002-0846-936X
M. G. Navarro https://orcid.org/0000-0002-1860-2304
A. Aloisi https://orcid.org/0000-0003-4137-882X
R. J. Rickards Vaught https://orcid.org/0000-0001-9719-4080
A. Adamo https://orcid.org/0000-0002-8192-8091
F. Annibali https://orcid.org/0000-0003-3758-4516
D. Calzetti https://orcid.org/0000-0002-5189-8004
S. Hernandez https://orcid.org/0000-0003-4857-8699
B. L. James https://orcid.org/0000-0003-4372-2006
M. Mingozzi https://orcid.org/0000-0003-2589-762X
R. Schneider https://orcid.org/0000-0001-9317-2888
M. Tosi https://orcid.org/0000-0002-0986-4759
B. Brandl https://orcid.org/0000-0001-9737-169X
M. G. del Valle-Espinosa https://orcid.org/0000-0002-0191-4897
F. Donnan https://orcid.org/0000-0002-6460-3682
A. S. Hirschauer https://orcid.org/0000-0002-2954-8622
M. Meixner https://orcid.org/0000-0002-0522-3743
D. Rigopoulou https://orcid.org/0000-0001-6854-7545

References

Akaike, H. 1974, ITAC, 19, 716
Aloisi, A., Clementini, G., Tosi, M., et al. 2007, ApJL, 667, L151
Aniano, G., Draine, B. T., Hunt, L. K., et al. 2020, ApJ, 889, 150
Annibali, F., Cignoni, M., Tosi, M., et al. 2013, AJ, 146, 144
Argyriou, I., Glasse, A., Law, D. R., et al. 2023, A&A, 675, A111
Astropy Collaboration, Price-Whelan, A. M., Sipőcz, B. M., et al. 2018, AJ, 156, 123
Astropy Collaboration, Robitaille, T. P., Tollerud, E. J., et al. 2013, A&A, 558, A33
Barker, A. S. 1963, PhRv, 132, 1474
Barone, L. T., Heithausen, A., Hüttemeister, S., Fritz, T., & Klein, U. 2000, MNRAS, 317, 649
Bertoldi, F., Draine, B. T., Rosenthal, D., et al. 2000, in IAU Symp. 197, From Molecular Clouds to Planetary, ed. Y. C. Minh & E. F. van Dishoeck (Cambridge: Cambridge Univ. Press), 191
Bolatto, A. D., Jackson, J. M., & Ingalls, J. G. 1999, ApJ, 513, 275
Bolatto, A. D., Wolfire, M., & Leroy, A. K. 2013, ARA&A, 51, 207
Bortolini, G., Östlin, G., Habel, N., et al. 2024, A&A, 689, A146
Bothwell, M. S., Maiolino, R., Kennicutt, R., et al. 2013, MNRAS, 433, 1425
Bron, E., Le Bourlot, J., & Le Petit, F. 2014, A&A, 569, A100
Bron, E., Le Petit, F., & Le Bourlot, J. 2016, A&A, 588, A27
Burton, M. G., Howe, J. E., Geballe, T. R., & Brand, P. W. J. L. 1998, PASA, 15, 194
Calabrò, A., Pentericci, L., Santini, P., et al. 2024, A&A, 690, A290
Cannon, J. M., Walter, F., Skillman, E. D., & van Zee, L. 2005, ApJL, 621, L21
Chastenet, J., Sandstrom, K., Chiang, I.-D., et al. 2019, ApJ, 876, 62
Chown, R., Leroy, A. K., Bolatto, A. D., et al. 2025, ApJ, 987, 91
Chown, R., Sidhu, A., Peeters, E., et al. 2024, A&A, 685, A75
Clark, I. Y., Sandstrom, K., Wolfire, M., et al. 2025, ApJ, 990, 209
Cormier, D., Madden, S. C., Lebouteiller, V., et al. 2014, A&A, 564, A121
Crowther, P. A., Schnurr, O., Hirschi, R., et al. 2010, MNRAS, 408, 731
Davies, R., Shimizu, T., Pereira-Santaella, M., et al. 2024, A&A, 689, A263
Dell'Agli, F., García-Hernández, D. A., Rossi, C., et al. 2014, MNRAS, 441, 1115
Draine, B. T. 2011, Physics of the Interstellar and Intergalactic Medium (Princeton, NJ: Princeton Univ. Press)
Draine, B. T., & Bertoldi, F. 1996, ApJ, 468, 269
Draine, B. T., & Hensley, B. 2013, ApJ, 765, 159
Draine, B. T., Li, A., Hensley, B. S., et al. 2021, ApJ, 917, 3
Draine, B. T., & Woods, D. T. 1990, ApJ, 363, 464
Dufour, R. J., & Hester, J. J. 1990, ApJ, 350, 149
Elmegreen, B. G., & Efremov, Y. N. 1997, ApJ, 480, 235
Engelbracht, C. W., Gordon, K. D., Rieke, G. H., et al. 2005, ApJL, 628, L29
Evans, C. J., Castro, N., Gonzalez, O. A., et al. 2019, A&A, 622, A129
Fabian, D., Henning, T., Jäger, C., et al. 2001, A&A, 378, 228
Fisher, D. B., Bolatto, A. D., Herrera-Camus, R., et al. 2014, Natur, 505, 186
Foreman-Mackey, D., Hogg, D. W., Lang, D., & Goodman, J. 2013, PASP, 125, 306
Fumagalli, M., Krumholz, M. R., & Hunt, L. K. 2010, ApJ, 722, 919
Furtak, L. J., Shuntov, M., Atek, H., et al. 2023, MNRAS, 519, 3064
Gaia Collaboration, Brown, A. G. A., Vallenari, A., et al. 2021, A&A, 649, A1

García-Bernete, I., Rigopoulou, D., Donnan, F. R., et al. 2024, A&A, 691, A162
Giacomazzi, L., Shcheblanov, N. S., Povarnitsyn, M. E., et al. 2023, PhRvM, 7, 045604
Glover, S. C. O., & Clark, P. C. 2012, MNRAS, 426, 377
Gondhalekar, P. M., Johansson, L. E. B., Brosch, N., Glass, I. S., & Brinks, E. 1998, A&A, 335, 152
Goodman, J., & Weare, J. 2010, CAMCS, 5, 65
Green, G. 2018, JOSS, 3, 695
Hamanowicz, A., Tchernyshyov, K., Roman-Duval, J., et al. 2024, ApJ, 966, 80
Harris, C. R., Millman, K. J., van der Walt, S. J., et al. 2020, Natur, 585, 357
Hassani, H., Rosolowsky, E., Leroy, A. K., et al. 2023, ApJL, 944, L21
Heintz, K. E., Giménez-Arteaga, C., Fujimoto, S., et al. 2023, ApJL, 944, L30
Hernandez, S., Jones, L., Smith, L. J., et al. 2023, ApJ, 948, 124
Hirschauer, A. S., Crouzet, N., Habel, N., et al. 2024, AJ, 168, 23
Hunt, L. K., Aloisi, A., Navarro, M. G., et al. 2025, ApJ, 992, 48, Paper I
Hunt, L. K., Dyer, K. K., & Thuan, T. X. 2005, A&A, 436, 837
Hunt, L. K., García-Burillo, S., Casasola, V., et al. 2015, A&A, 583, A114
Hunt, L. K., Testi, L., Casasola, V., et al. 2014, A&A, 561, A49
Hunt, L. K., Thuan, T. X., Izotov, Y. I., & Sauvage, M. 2010, ApJ, 712, 164
Hunt, L. K., Tortora, C., Ginolfi, M., & Schneider, R. 2020, A&A, 643, A180
Izotov, Y. I., Chaffee, F. H., Foltz, C. B., et al. 1999, ApJ, 527, 757
Jäger, C., Mutschke, H., & Henning, T. 1998, A&A, 332, 291
Janowiecki, S., Salzer, J. J., van Zee, L., Rosenberg, J. L., & Skillman, E. 2017, ApJ, 836, 128
Kavanagh, S., Squires, A., Nicolson, A., et al. 2024, JOSS, 9, 6433
Koike, C., Kaito, C., Yamamoto, T., et al. 1995, Icar, 114, 203
Koike, C., Matsuno, J., & Chihara, H. 2017, ApJ, 845, 115
Kruijssen, J. M. D. 2015, MNRAS, 454, 1658
Krumholz, M. R. 2012, ApJ, 759, 9
Lai, T. S. Y., Armus, L. U. V., et al. 2022, ApJL, 941, L36
Law, D. R., Argyriou, I., Gordon, K. D., et al. 2025, AJ, 169, 67
Le Bourlot, J., Le Petit, F., Pinto, C., Roueff, E., & Roy, F. 2012, A&A, 541, A76
Le Petit, F., Nehmé, C., Le Bourlot, J., & Roueff, E. 2006, ApJS, 164, 506
Law, D. R., E. Morrison, J., Argyriou, I., et al. 2023, AJ, 166, 45
Lelli, F., Verheijen, M., Fraternali, F., & Sancisi, R. 2012, A&A, 537, A72
Leroy, A., Cannon, J., Walter, F., Bolatto, A., & Weiss, A. 2007, ApJ, 663, 990
Madden, S. C., Galliano, F., Jones, A. P., & Sauvage, M. 2006, A&A, 446, 877
Madden, S. C., Rémy-Ruyer, A., Galametz, M., et al. 2014, PASP, 126, 1079
Marassi, S., Schneider, R., Limongi, M., et al. 2019, MNRAS, 484, 2587
McDonald, I., Boyer, M. L., van Loon, J. T., & Zijlstra, A. A. 2011, ApJ, 730, 71
McDonald, I., Sloan, G. C., Zijlstra, A. A., et al. 2010, ApJL, 717, L92
Meyer, D. M., Lauroesch, J. T., Sofia, U. J., Draine, B. T., & Bertoldi, F. 2001, ApJL, 553, L59
Morishita, T., Stiavelli, M., Grillo, C., et al. 2024, ApJ, 971, 43
Nanni, A., Burgarella, D., Theulé, P., Côté, B., & Hirashita, H. 2020, A&A, 641, A168
Ossenkopf, V., Henning, T., & Mathis, J. S. 1992, A&A, 261, 567
Ott, J., Walter, F., & Brinks, E. 2005, MNRAS, 358, 1423
Peeters, E., Habart, E., Berné, O., et al. 2024, A&A, 685, A74
Pereira-Santaella, M., Spinoglio, L., van der Werf, P. P., & Piqueras López, J. 2014, A&A, 566, A49
Popping, G., Somerville, R. S., & Trager, S. C. 2014, MNRAS, 442, 2398
Posch, T., Kerschbaum, F., Mutschke, H., et al. 1999, A&A, 352, 609
Rémy-Ruyer, A., Madden, S. C., Galliano, F., et al. 2014, A&A, 563, A31
Rhoads, J. E., Wold, I. G. B., Harish, S., et al. 2023, ApJL, 942, L14
Rickards Vaught, R. J., Hunt, L. K., Aloisi, A., et al. 2025, ApJ, 990, 111, Paper III
Rickards Vaught, R. J., Sandstrom, K. M., & Hunt, L. K. 2021, ApJL, 911, L17
Rigby, J., Perrin, M., McElwain, M., et al. 2023, PASP, 135, 048001
Rigopoulou, D., Barale, M., Clary, D. C., et al. 2021, MNRAS, 504, 5287
Rigopoulou, D., Donnan, F. R., García-Bernete, I., et al. 2024, MNRAS, 532, 1598
Roueff, E., Abgrall, H., Czachorowski, P., et al. 2019, A&A, 630, A58
Rouleau, F., & Martin, P. G. 1991, ApJ, 377, 526
Rubio, M., Elmegreen, B. G., Hunter, D. A., et al. 2015, Natur, 525, 218
Sandstrom, K. M., Bolatto, A. D., Bot, C., et al. 2012, ApJ, 744, 20
Schinnerer, E., & Leroy, A. K. 2024, ARA&A, 62, 369
Schneider, R., & Maiolino, R. 2024, A&ARv, 32, 2
Shi, Y., Wang, J., Zhang, Z.-Y., et al. 2020, ApJ, 892, 147
Sloan, G. C., Kraemer, K. E., Goebel, J. H., & Price, S. D. 2003, ApJ, 594, 483
Sternberg, A., & Neufeld, D. A. 1999, ApJ, 516, 371
Takigawa, A., Stroud, R. M., Nittler, L. R., O'D Alexander, C. M., & Miyake, A. 2018, ApJL, 862, L13
Telford, O. G., Sandstrom, K. M., McQuinn, K. B. W., et al. 2024, arXiv:2410.21368
Thuan, T. X., Bauer, F. E., Papaderos, P., & Izotov, Y. I. 2004, ApJ, 606, 213
Togi, A., & Smith, J. D. T. 2016, ApJ, 830, 18
Toribio San Cipriano, L., Domínguez-Guzmán, G., Esteban, C., et al. 2017, MNRAS, 467, 3759
Trump, J. R., Arrabal Haro, P., Simons, R. C., et al. 2023, ApJ, 945, 35
Valdivia-Mena, M. T., Rubio, M., Kalari, V. M., et al. 2025, A&A, 699, A369
van Dishoeck, E. F., & Black, J. H. 1988, ApJ, 334, 771
van Zee, L., Westpfahl, D., Haynes, M. P., & Salzer, J. J. 1998, AJ, 115, 1000
Vanzella, E., Loiacono, F., Bergamini, P., et al. 2023, A&A, 678, A173
Vanzella, E., Loiacono, F., Messa, M., et al. 2024, A&A, 691, A251
Virtanen, P., Gommers, R., Oliphant, T. E., et al. 2020, NatMe, 17, 261
Walter, F., Carilli, C., Neeleman, M., et al. 2020, ApJ, 902, 111
Wang, Y., Muramatsu, A., & Sugimoto, T. 1998, ColSu, 134, 281
Wolfire, M. G., Hollenbach, D., & McKee, C. F. 2010, ApJ, 716, 1191
Zakamska, N. L. 2010, Natur, 465, 60
Zeidler, S., Posch, T., & Mutschke, H. 2013, A&A, 553, A81
Zhou, L., Shi, Y., Zhang, Z.-Y., & Wang, J. 2021, A&A, 653, L10
Zubko, V. G., Mennella, V., Colangeli, L., & Bussoletti, E. 1996, MNRAS, 282, 1321